

UCI

University of California, Irvine

Microsystems Laboratory
Technical Report

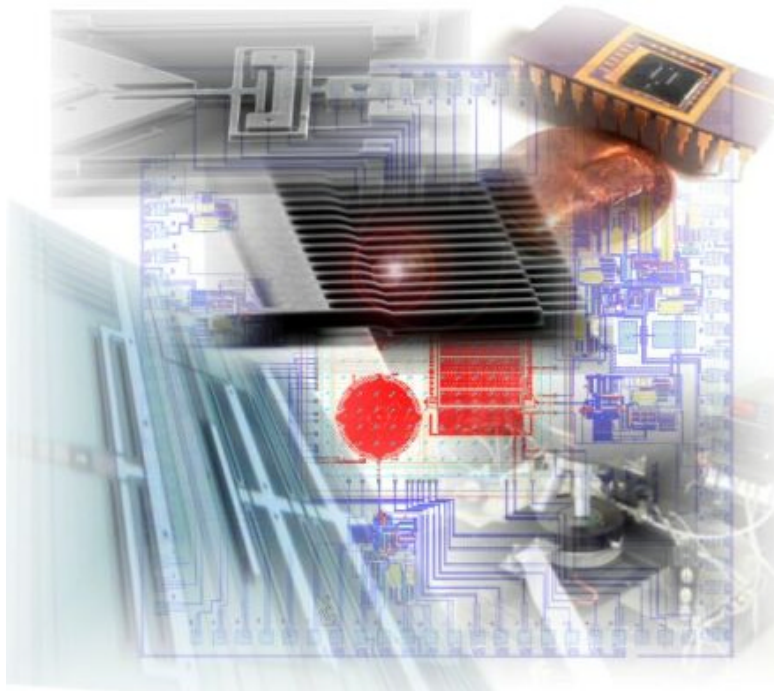


Design Concept and Preliminary Experimental Demonstration of 4-DOF MEMS Gyroscopes

Cenk Acar

March 7, 2002

Technical Report No: MSL-01006



MICRO  SYSTEMS
LABORATORY

UNIVERSITY OF CALIFORNIA

IRVINE

FOUR DEGREES-OF-FREEDOM MICROMACHINED GYROSCOPE

QUALIFYING EXAMINATION REPORT

Cenk Acar

Mechanical and Aerospace Engineering

Examination Committee:

Professor Andrei M. Shkel, Chair

Professor James E. Bobrow

Professor Athanassios Sideris

Professor Kenneth D. Mease

Professor Abe Lee

Contents

List of Figures	iv
Abstract	viii
1 Introduction	1
1.1 Research Motivation	1
1.2 Outline	2
1.3 Micro-Electro-Mechanical Gyroscopes	2
1.3.1 Prior Work	3
1.4 Conventional Micromachined Gyroscope Design Approach	3
1.4.1 Gyroscope Dynamics	4
1.4.2 A Generic MEMS Implementation	6
1.4.3 The Coriolis Response	7
1.4.4 Mode-Matching Problem	8
1.4.5 Phase Relations and Proof-Mass Trajectory	9
1.4.6 Anisoelasticity and Quadrature Error Issues	11
1.4.7 Conclusion	13
2 The 4-DOF Design Approach for MEMS Gyroscope	14
2.1 Design Approach and Principle of Operation	14
2.1.1 The Design Basics	15
2.1.2 Principle of Operation	15
2.2 Gyroscope Dynamics	16
2.3 Phase Relations and Effects of Anisoelasticity	18
3 MEMS Implementation of the Design Concept	21
3.1 Mechanical Design	21
3.1.1 Suspension Design	21

3.1.2	Damping Estimation	23
3.2	Electrical Design	26
3.2.1	Electrostatic Actuation	27
3.2.2	Electrostatic Sensing	28
3.3	Dynamic Amplification in Drive Mode	29
3.4	Parameter Optimization for Improved Performance	31
3.5	Alternative Design Implementations	33
4	Parametric Sensitivity Analysis	35
4.1	Fabrication Variations	35
4.2	Pressure Fluctuations	38
4.3	Thermal Fluctuations	39
4.4	Residual Stresses	41
4.5	Conclusion	42
5	Preliminary Experimental Results	43
5.1	Fabrication of a Prototype	43
5.1.1	MUMPs Surface Micromachining Process	44
5.1.2	Design Implementation Using MUMPs Technology	45
5.2	The Experimental Setup	47
5.3	Preliminary Experimental Verification of the Design Concept	48
5.4	Conclusion	50
6	Conclusion and Research Goals	51
6.1	Summary of Achievements	51
6.2	Future Goals	52

List of Figures

1.1	Comparison of the single-mass conventional gyroscopes and the proposed 4-DOF system.	1
1.2	A conventional rate gyroscope has a single proof mass which is free to oscillate in two principle directions: drive and sense.	4
1.3	Time derivative of a vector in a rotating frame.	5
1.4	Schematic illustration of the inertial frame and the rotating gyroscope frame.	6
1.5	MEMS implementation of a conventional rate gyroscope.	6
1.6	The response of the system can be viewed as a 1-DOF system excited by the Coriolis force. Note that the gain is very sensitive to matching of drive and sense mode resonant frequencies, as well as damping fluctuations.	7
1.7	The response of the overall 2-DOF system with varying drive and sense stiffness mismatch. The highest response corresponds to the case where the drive and sense modes are matched, and the response amplitude diminishes as the mismatch increases.	8
1.8	(a) The oscillation pattern when $\omega_d = \omega_y$. (b) The oscillation pattern when $\omega_d \neq \omega_y$. (c) Phase relations in x and y directions. Note that, the phase difference $\phi_y - \phi_x$ does not depend on the the drive direction resonant frequency ω_x . The phase difference is determined solely by $\omega_d - \omega_y$	10
1.9	The ellipticity of the straight line of oscillation grows as the driving frequency ω_d deviates from the sense direction resonant frequency ω_y	11
1.10	(a) Deviation of the elliptic oscillation pattern due to increasing anisoelasticity. (b) Effect of anisoelasticity on the straight line of oscillation along x -axis with zero input rotation rate. (c) In the absence of input rate, anisoelasticity induces a sense direction response similar to the Coriolis response.	12
1.11	Effect of anisoelasticity on (a) stiffness mismatched systems, and (b) systems with ω_d deviated from ω_y	13

2.1	Lumped mass-spring-damper model of the dual-mass gyroscope. The first mass is driven in the x direction, and the response of the second mass along the y-axis is sensed.	14
2.2	Schematic illustration of a MEMS implementation of the dual-mass z-axis gyroscope.	15
2.3	Response of the dual-mass gyroscope in the flat operation region is insensitive to resonant frequency fluctuations and has over 15 times wider bandwidth than in conventional gyroscopes.	16
2.4	(a) Representation of the position vector of a body relative to the rotating frame. (b) Representation of the position vectors of the proof masses of the gyroscope relative to the rotating "gyroscope frame" B.	17
2.5	The 4-DOF dynamical system observed in the rotating gyroscope frame.	18
2.6	Modeling of asymmetric imperfections in the 4-DOF gyroscope. The asymmetric imperfections can be modeled as an angle of elasticity ε_1 for substrate-active mass suspension, and ε_2 for active mass-passive mass suspension.	19
2.7	Oscillation patterns variation of the active and passive masses with (a) increasing ε_1 and (b) increasing ε_2	20
2.8	Effect of(a) ε_1 variation, and (b) ε_2 variation on 4-DOF system response.	20
3.1	Illustration of the proposed dual-mass z-axis micromachined gyroscope design. . . .	22
3.2	The fixed-guided end beam deflection.	22
3.3	Suspension system configuration provides two degrees of freedom (in drive and sense directions) for the active proof mass and the passive proof mass.	23
3.4	The first three resonant modes of the gyroscope. The simulation is performed using the finite element analysis package ANSYS. FEA results agree with the theoretical analysis within 0.1% error.	24
3.5	Illustration of Couette flow damping between two plates, where the plates slide along each other.	25
3.6	Illustration of Squeeze-film damping between two plates, where the plates move towards each other.	25
3.7	The capacitance between two plates.	27
3.8	(a) The comb-drive structure for electrostatic actuation. (b) The balanced comb-drive scheme.	27
3.9	The microscope photograph of the comb-drives attached to the first mass in the fabricated prototype z-axis dual-mass gyroscope.	28

3.10	The differential air-gap sense capacitors for response sensing.	28
3.11	Air-gap sense capacitors attached to the second mass in the fabricated prototype z-axis dual-mass gyroscope.	29
3.12	Lumped model of the drive mode of dual-mass gyroscope. The passive mass (m_2) amplifies the motion of the active mass (m_1).	30
3.13	(a) The magnitude plots of each proof mass. At the antiresonant frequency, which is the resonant frequency of the isolated passive mass-spring system, oscillation am- plitude of the active mass approaches to zero. (b) The phase plots of the proof masses.	30
3.14	(a) The dynamic amplification ratio reaches its maximum at the antiresonant fre- quency, i.e., $\omega_{drive} = \sqrt{\frac{k_{2x}}{m_2}}$. (b) With a balanced interdigitated comb-drive scheme, a $1\mu m$ amplitude is achieved by the passive mass with a bias voltage of about 20V. .	31
3.15	Effect of (a) passive mass m_2 variation, and (b) antiresonant frequency ω_{22} variation on drive direction response.	32
3.16	Effect of (a) mass ratio $\mu = m_2/m_1$ variation, and (b) frequency ratio $\gamma = \omega_{22}/\omega_{11}$ variation on drive direction response.	32
3.17	Effect of damping on drive direction response. When the damping is under a critical value, the response in the flat region is insensitive to pressure changes.	33
3.18	Torsional implementation of the 4-DOF design approach.	34
4.1	Fabrication variations can affect the geometry of the device by varying thickness of the structure or the width of the suspension beam elements. The proposed design illustrated in (b) is demonstrated to be more robust against these variations than the conventional approach illustrated in (a).	36
4.2	Change in the response due to: (a) $0.05\mu m$ variation in the width of suspension beams, (b) $0.1\mu m$ variation in thickness of the structure, (c) 10 GPa variation in Young's Modulus.	37
4.3	Damping changes have insignificant effect on response in the flat operation region. .	38
4.4	(a) Ambient pressure change from 100 millitorrs to 500 millitorrs results in 2% gain reduction for the proposed gyroscope design, (b) The same pressure change causes over 60% gain reduction for a conventional gyroscope design with similar geometry.	38

4.5	(a) Finite element simulation of the device with a uniform temperature loading of $100^{\circ}C$. Thermally induced localized stresses were observed only in the drive-direction beam elements of active mass, effecting only k_{1x} . (b) Static finite element analysis of the thermally loaded system with the modified Young's modulus. (c) Finite element analysis of a conventional gyroscope with similar geometry, under the same thermal loading. (d) Static analysis of the conventional design indicate the localized stresses leading to frequency mismatch between the drive and the sense resonant frequencies.	40
4.6	(a) Simulation of the proposed design's dynamical system with the perturbed parameters due to thermal loading, indicating less than 0.9% gain deviation. (b) Simulation of the conventional design with the perturbed parameters indicates 7% gain error for the same thermal loading.	41
4.7	Effect of residual stresses from -10MPa to 10MPa (a) in x-direction, (b) in y-direction.	42
5.1	Cross-section of a device fabricated using the first two structural layers of MUMPs micromachining process [25].	43
5.2	The fabrication steps of the three-layer MUMPs technology.	44
5.3	Scanning Electron Microscope (SEM) photograph of (a) the comb-drives, and (b) the air-gap sense capacitors.	45
5.4	(a) The detailed view of the dual-mass z-axis gyroscope layout. (b) The microscope photograph of the gyroscope prototype.	46
5.5	The layout of the dual-mass z-axis gyroscope.	47
5.6	Experimental setup for experimental evaluation of prototype gyroscopes.	47
5.7	Scanning Electron Microscope (SEM) photograph of the tested prototype gyroscope.	48
5.8	Experimental verification of the wide constant-amplitude operation frequency band. 4-DOF system provides a constant-amplitude oscillation frequency band over 10 times larger than conventional gyroscopes under same operation conditions.	49
5.9	Demonstration of mechanical amplification in drive direction. The oscillation blur of the passive mass is highlighted on the left. At the antiresonance frequency, the passive mass amplitude is over an order of magnitude larger than the active mass amplitude.	50
6.1	a two-chip solution where a capacitive sensing chip in the die form is packaged together with the gyroscope die.	53

ABSTRACT

Four Degrees-of-Freedom Micromachined Gyroscope

by

Cenk Acar

Mechanical and Aerospace Engineering

University of California, Irvine, 2002

Advisor: Professor Andrei M. Shkel

This Ph.D. research focuses on exploration of a novel design concept for MEMS gyroscopes. The approach is based on expanding the system design space by increasing the degrees-of-freedom (DOF) of the oscillatory system with the integration of two independently oscillating interconnected proof masses. Detailed modeling and preliminary experimental characterization indicate inherent robustness of the proposed system against fabrication variations, and fluctuations in the ambient temperature or pressure during the operation time of the device. With the new design approach, passive disturbance-rejection is achieved by the mechanical system. Thus, the concept provides a paradigm shift in design of MEMS gyroscopes from the complexity of the control electronics to expanded dimensionality of the system design space.

In this report, in order to form a basis of comparison between the conventional and 4-DOF gyroscopes, first a detailed analysis of the conventional gyroscope dynamics together with investigation of oscillation pattern issues affected by phase relations and anisoelectricity in the suspension structure is presented. Followed by the introduction of 4-DOF gyroscope design concept along with system dynamics and MEMS implementation basics, an approach for determining optimal system parameters to maximize sensor performance is presented. The phase relations in the ideal and non-ideal 4-DOF system is also analyzed to obtain mass trajectories in order to compare with the conventional systems from the Quadrature control point of view. For demonstration of the improved robustness of the proposed system, the effects of realistic parameter variations on the system response are investigated, and the sensitivity of the proposed system to these variations is compared to the conventional design approach. Preliminary experimental results verifying the major operational principles of the 4-DOF gyroscope are also presented together with the details on the fabricated prototype devices. Finally, future research objectives leading to the completion of the thesis are highlighted.

Chapter 1

Introduction

In this chapter, a general overview of conventional micromachined gyroscopes, and their operation principle is presented. Analysis of the dynamics, Coriolis response and implementation basics of the micromachined vibratory rate gyroscopes is followed by discussion of the limitations of the conventional approach, which defines the motivation of this research.

1.1 Research Motivation

The current state of the art micromachined gyroscopes require an order of magnitude improvement in performance, stability, and robustness. Fabrication variations and fluctuations in the ambient temperature or pressure during the operation time of these devices introduce significant errors, which have to be compensated by sophisticated control electronics. To eliminate the limitations of the existing micromachined gyroscopes including high sensitivity to variations in system parameters and narrow bandwidth, complexity of the control electronics can be shifted to complexity in the dynamical system.

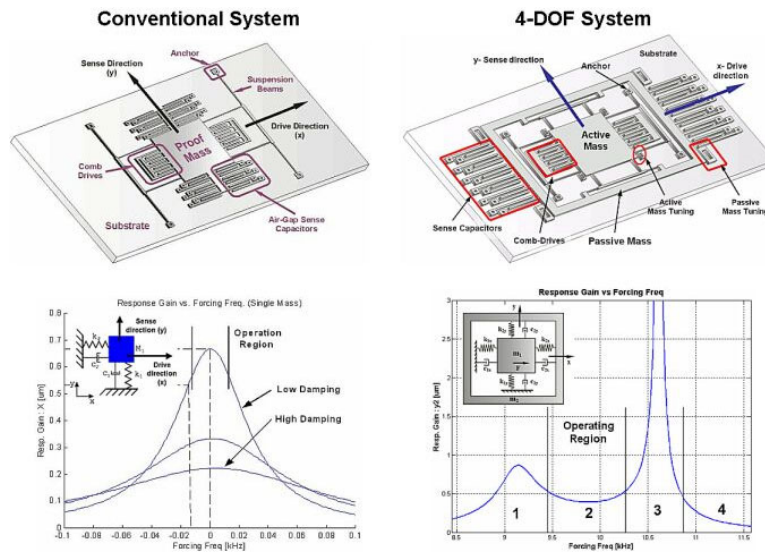


Figure 1.1: Comparison of the single-mass conventional gyroscopes and the proposed 4-DOF system.

The objective of this research is to develop a new dynamical system design approach for gyroscopes, which will have inherent robustness against parameter variations, and require less demanding active compensation schemes. The proposed design concept suggests the use of two coupled independently vibrating proof masses to form a 4-DOF dynamical system. Computer modeling and experimental results indicated over 15 times increase in the bandwidth of the system as compared to the conventional gyroscopes (Fig. 1.1). In addition, significantly reduced sensitivity of the gyroscope to structural and thermal parameter fluctuations and damping is demonstrated.

1.2 Outline

In Chapter 1, conventional micromachined gyroscopes are analyzed in detail in order to point out their drawbacks defining the research motivation. In Chapter 2, the 4-DOF micromachined vibratory rate gyroscope design approach is presented along with the principle of operation, system dynamics, and the phase relations in the ideal and non-ideal system. Chapter 3 describes the basics of a MEMS implementation of the design concept, with an approach for determining optimal system parameters for improved performance. In Chapter 4, sensitivity of the proposed micromachined gyroscope design to realistic variations in system parameters is analyzed to compare with the conventional designs. Then, the preliminary experimental results verifying the major operational principles of the 4-DOF gyroscope are presented in Chapter 5 along with an overview of the used fabrication technology and the experimental setup. Finally, in Chapter 6, a brief summary of achievements is given, and the future goals of the research are stated.

1.3 Micro-Electro-Mechanical Gyroscopes

Even though there is an extensive variety of micromachined gyroscope designs and operation principles, almost all of the reported micromachined gyroscopes use vibrating mechanical elements to sense rotation. The vibrating mechanical elements have no rotating parts that require bearings, and hence they can be batch fabricated in micromachining processes. All vibratory gyroscopes are based on the transfer of energy between two vibration modes of a structure caused by Coriolis acceleration, which is induced due to an input rotation rate.

Micromachined gyroscopes for measuring rate or angle of rotation can be used in a wide spectrum of areas including automotive applications for ride stabilization and roll-over detection; some consumer electronic applications, such as video-camera stabilization, virtual reality, and inertial mouse for computers, robotics applications, and a wide range of military applications; or to provide position information in inertial navigation systems together with micromachined accelerometers.

Precision fiber-optic gyroscopes, ring laser gyroscopes, and conventional rotating wheel gyroscopes are too expensive and too large for use in most emerging applications. With micromachining technologies, sensor size is reduced by orders of magnitude, and fabrication cost is dropped significantly. Moreover, advances in the fabrication techniques allow the electronics to be integrated on the same silicon chip together with the mechanical components.

1.3.1 Prior Work

Various micromachined gyroscope designs fabricated in surface micromachining, bulk micromachining, hybrid surface-bulk micromachining technologies or alternative fabrication techniques have been reported throughout the last decade. A detailed review of these designs can be found in [1, 2, 4]. However, commercially available MEMS gyroscopes are still scarce.

In recent years, a number of gyroscope designs with multiple proof-masses and different operation principles have been proposed for improving performance and robustness of MEMS gyroscopes [7, 8, 9, 13, 14, 15, 16]. Most of these designs rely on limiting the degrees-of-freedom of the driven mass to only the drive direction. In these designs, either a part of the Coriolis Force induced on the driven mass is transferred to the sensing mass while suppressing the motion of the sensing mass in drive direction [7, 9, 13, 14]; or the drive direction oscillation of the driven mass is transferred to the sensing mass while the driven mass is not allowed to oscillate in the sense direction [8, 15, 16]. These designs are still virtually two degrees-of-freedom systems, however, they offer various advantages from the drive and sense mode decoupling and mode-matching points of view.

Multiple degrees-of-freedom resonators providing larger drive-direction amplitudes for improving the performance of vibratory MEMS devices have also been recently reported [10, 11, 12, 17, 19]. Two degrees-of-freedom oscillators utilizing mechanical amplification of motion for large oscillation amplitudes have been proposed, however, no results on integration of this oscillator system into MEMS gyroscopes have been indicated [10, 11, 12].

1.4 Conventional Micromachined Gyroscope Design Approach

In this section, the basic operational principles of conventional micromachined vibratory rate gyroscopes are analyzed in order to highlight the drawbacks of the conventional approach, which can be overcome by the 4-DOF design concept. First, the dynamics of the vibratory gyroscopes is developed, then the MEMS implementation basics are presented. Also the response characteristics and oscillation patterns of the gyroscope to the rotation-induced Coriolis force are analyzed considering phase relations issues and anisoelectricity in the suspension structure.

1.4.1 Gyroscope Dynamics

Almost all existing micromachined rate gyroscopes operate on the vibratory principle of a single proof mass suspended above the substrate. The proof mass is free to oscillate in two orthogonal directions (Fig. 1.2): the drive direction (x-Axis) and the sense direction (y-Axis) [1]. The overall dynamical system is simply a two degrees-of-freedom (2-DOF) mass-spring-damper system.

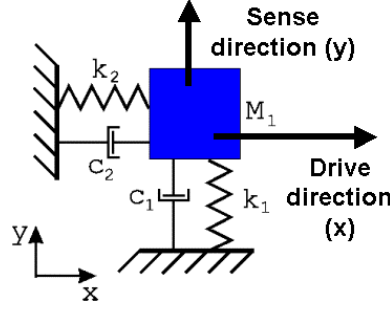


Figure 1.2: A conventional rate gyroscope has a single proof mass which is free to oscillate in two principle directions: drive and sense.

The principle of operation can be best understood by considering the rotation-induced Coriolis force acting on a body observed in a rotating reference frame. The accelerations experienced by a moving body in a rotating reference frame can be calculated having the following definitions:

FrameA : Inertial frame

FrameB : Rotating reference frame

\vec{r}_A : Position vector relative to inertial frame A

\vec{r}_B : Position vector relative to rotating frame B

$\vec{\theta}$: Orientation of rotating frame B

\vec{R} : Position of rotating frame B,

and the time derivative of a vector \vec{r} , which is defined in two reference frames *A*, and *B* as $\dot{\vec{r}}_A$, and $\dot{\vec{r}}_B$, respectively, is given as

$$\dot{\vec{r}}_A(t) = \dot{\vec{r}}_B(t) + \dot{\vec{\theta}} \times \vec{r}_B(t). \quad (1.1)$$

Taking the second time derivative of the position vector \vec{r} , the accelerations of a body moving with the rotating reference frame can be calculated as:

$$\ddot{\vec{r}}_A(t) = \ddot{\vec{R}}(t) + \ddot{\vec{r}}_B(t) \quad (1.2)$$

$$\dot{\vec{r}}_A(t) = \dot{\vec{R}}(t) + \dot{\vec{r}}_B(t) + \dot{\vec{\theta}} \times \vec{r}_B(t) \quad (1.3)$$

$$\ddot{\vec{r}}_A(t) = \ddot{\vec{R}}(t) + \ddot{\vec{r}}_B(t) + \dot{\vec{\theta}} \times \dot{\vec{r}}_B(t) + \dot{\vec{\theta}} \times (\dot{\vec{\theta}} \times \vec{r}_B(t)) + \ddot{\vec{\theta}} \times \vec{r}_B(t) + \dot{\vec{\theta}} \times \dot{\vec{r}}_B(t). \quad (1.4)$$

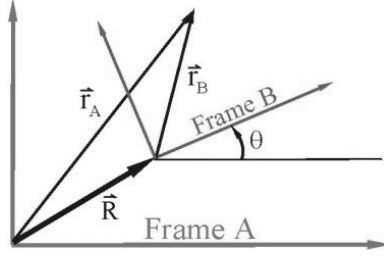


Figure 1.3: Time derivative of a vector in a rotating frame.

With the definition of \vec{v}_B and \vec{a}_B as the velocity and acceleration vectors with respect to the reference frame, \vec{a}_A as the acceleration vector with respect to the inertial frame, \vec{A} as the linear acceleration of the reference frame, and $\vec{\Omega}$ as the angular velocity of the rotating frame; the expression for acceleration reduces to:

$$\vec{a}_A = \vec{A} + \vec{a}_B + \vec{\Omega} \times \vec{r}_B + \vec{\Omega} \times (\vec{\Omega} \times \vec{r}_B) + 2\vec{\Omega} \times \vec{v}_B. \quad (1.5)$$

The last term $2\vec{\Omega} \times \vec{v}_B$ in the equation is called the Coriolis term. This acceleration term is of special interest since the rotation rate of the rotating reference frame B can be deduced by measuring the Coriolis acceleration. Consequently, the rate gyroscopes can be viewed as an accelerometer measuring the Coriolis acceleration to calculate the rotation rate.

When the acceleration vector of the proof mass is expressed with respect to the inertial frame A by taking the second time derivative of the position vector (Figure 1.4), the equation of motion become

$$\vec{F}_{ext} = m(\vec{A} + \vec{a}_B + \vec{\Omega} \times \vec{r}_B + \vec{\Omega} \times (\vec{\Omega} \times \vec{r}_B) + 2\vec{\Omega} \times \vec{v}_B) \quad (1.6)$$

where \vec{A} is the linear acceleration and $\vec{\Omega}$ is the angular velocity of the rotating gyroscope frame, \vec{v}_B and \vec{a}_B are the velocity and acceleration vectors of the proof mass with respect to the reference frame, and \vec{F}_{ext} is the total external force applied to the proof mass.

If the motion is decomposed into the two principle oscillation directions, the drive and the sense directions, and if the linear accelerations are negligible or cancelled out by the control system, the two equations of motion can be expressed as

$$\begin{aligned} m\ddot{x} + c_x\dot{x} + (k_x - m(\Omega_y^2 + \Omega_z^2))x + m(\Omega_x\Omega_y - \dot{\Omega}_z)y &= \tau_x + 2m\Omega_z\dot{y} \\ m\ddot{y} + c_y\dot{y} + (k_y - m(\Omega_x^2 + \Omega_z^2))y + m(\Omega_x\Omega_y + \dot{\Omega}_z)x &= \tau_y - 2m\Omega_z\dot{x}. \end{aligned} \quad (1.7)$$

For a constant angular rate input $\dot{\Omega}_z = 0$, and for angular rates much smaller than the driving frequency of the gyroscope, the terms Ω_x^2 , Ω_y^2 , and $\Omega_x\Omega_y$ can be neglected; resulting in the simplified 2-DOF equations of motion:

$$\begin{aligned} m\ddot{x} + c_x\dot{x} + k_x x &= \tau_x + 2m\Omega_z\dot{y} \\ m\ddot{y} + c_y\dot{y} + k_y y &= \tau_y - 2m\Omega_z\dot{x}. \end{aligned} \quad (1.8)$$

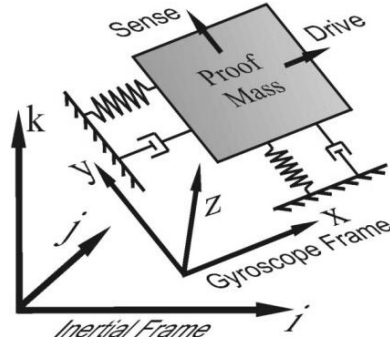


Figure 1.4: Schematic illustration of the inertial frame and the rotating gyroscope frame.

The two final terms $2m\Omega_z\dot{y}$, and $2m\Omega_z\dot{x}$ in the equation are the rotation-induced Coriolis forces, which cause dynamic coupling between the oscillation axes, and which are used for angular rate measurement.

1.4.2 A Generic MEMS Implementation

Most of the reported micromachined vibratory rate gyroscopes have a single proof mass suspended above the substrate. The proof mass is supported by anchored flexures, which serve as the flexible suspension between the proof mass and the substrate, making the mass free to oscillate in two orthogonal directions - the drive and the sense [1].

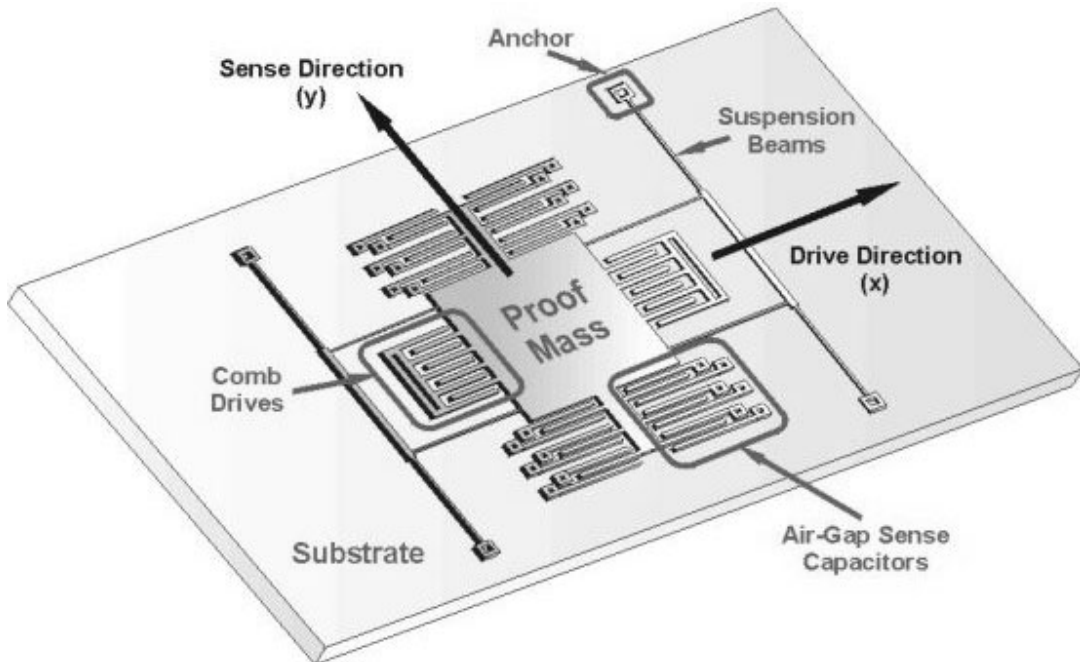


Figure 1.5: MEMS implementation of a conventional rate gyroscope.

The proof mass is driven into resonance in the drive direction by an external sinusoidal force. The external force is generally the electrostatic forces applied by comb-drive structures

(Figure 1.5), covered in Section 3.2.1. If the gyroscope is subjected to an angular rotation, the Coriolis force is induced in the y-direction. If the drive and sense resonant frequencies are matched, the Coriolis force excites the system into resonance in the sense direction. The resulting oscillation amplitude in the sense direction is proportional to the Coriolis force and, thus, to the angular velocity to be measured [3]. The sense direction oscillation is detected generally by air-gap capacitors (Figure 1.5), which is covered in Section 3.2.2, as well.

1.4.3 The Coriolis Response

To achieve the maximum possible gain, the conventional gyroscopes are generally designed to operate at or near the peak of the response curve. This is typically achieved by matching drive and sense resonant frequencies (Fig. 1.7). However, the system is very sensitive to variations in system parameters causing a shift in the resonant frequency.

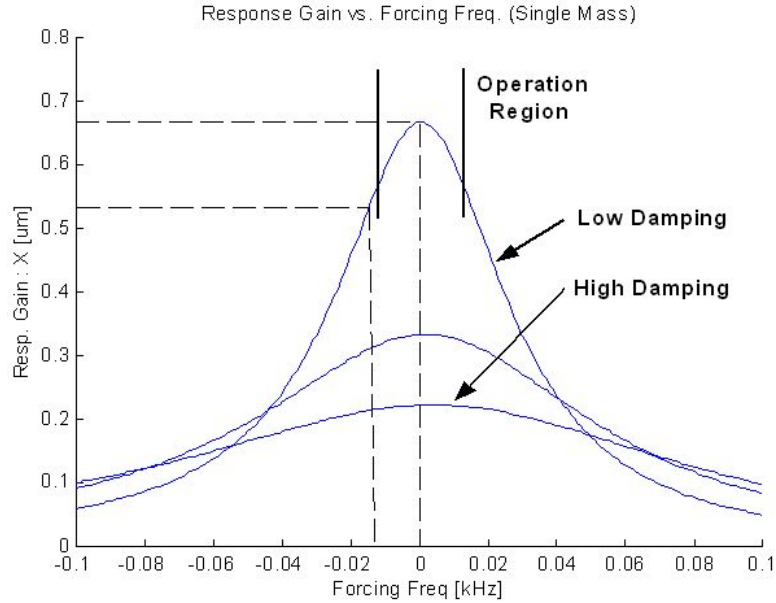


Figure 1.6: The response of the system can be viewed as a 1-DOF system excited by the Coriolis force. Note that the gain is very sensitive to matching of drive and sense mode resonant frequencies, as well as damping fluctuations.

Under high quality factor conditions the gain is high, however, the bandwidth is extremely narrow. For example, 1% fluctuation in frequency matching between drive and sense modes will produce an error of 20% in the output signal gain [18]. In addition, the gain is affected significantly by fluctuations in damping conditions (Figure 1.7).

Fabrication imperfections are inevitable, and affect material properties and geometry of MEMS structures. For surface micromachining, the thickness of the suspension elements is determined by deposition process, and the width is affected by etching process. In addition, Young's Modulus of the structure is affected by deposition conditions [2]. Variations in these

parameters have drastic effect on dynamic response of gyroscopes. Generally, very sophisticated control electronics is used to provide operation in the region of the resonance peak [5]. Furthermore, during the operation time of these devices, fluctuations in the ambient temperature and pressure introduce significant errors (Figure 1.7).

1.4.4 Mode-Matching Problem

A better insight to the dynamics of the single-mass 2-DOF gyroscope can be acquired by starting with the assumption that the system is driven without feedback control in drive direction x with a constant amplitude drive force F_d at the drive frequency ω_d , namely $F_d = F_o \sin \omega_d t$. For a constant angular rate input, i.e. $\dot{\Omega}_z = 0$, and for angular rates much lower than the driving frequency of the gyroscope, the equations of motion reduce to:

$$\begin{aligned} m\ddot{x} + c_x\dot{x} + k_x x &= F_o \sin \omega_d t + 2m\Omega_z \dot{y} \\ m\ddot{y} + c_y\dot{y} + k_y y &= -2m\Omega_z \dot{x}. \end{aligned} \quad (1.9)$$

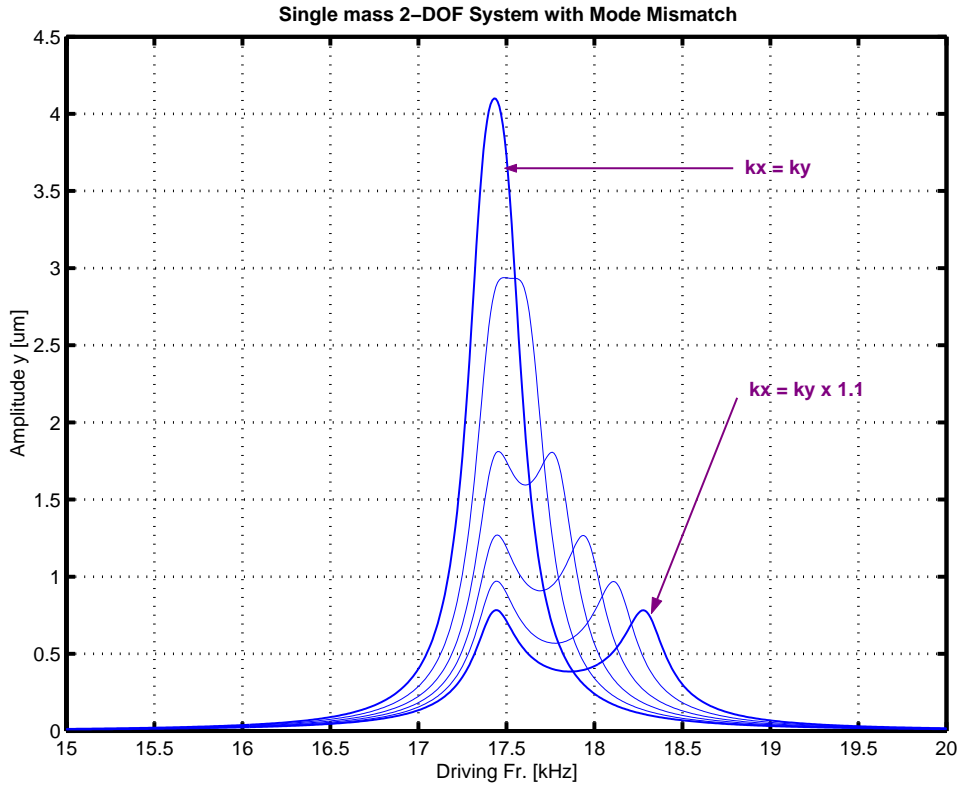


Figure 1.7: The response of the overall 2-DOF system with varying drive and sense stiffness mismatch. The highest response corresponds to the case where the drive and sense modes are matched, and the response amplitude diminishes as the mismatch increases.

The 2-DOF dynamical system will have two independent resonant frequencies: drive direction resonant frequency $\omega_x = \sqrt{k_x/m}$, and sense direction resonant frequency $\omega_y = \sqrt{k_y/m}$.

When the stiffness values in the drive and sense directions are the same, i.e. $k_x = k_y$ then the two resonance modes will be matched, i.e. $\omega_x = \omega_y$. However, fabrication imperfections are inevitable, and both the geometry and the material properties of MEMS devices are affected by etching processes, deposition conditions, and residual stresses, drastically affecting the suspension stiffness. Experimental results demonstrated a possible deviation of over 20% from the designed stiffness values. Generally, sophisticated control electronics is used to tune the resonance frequencies for mode-matching.

The rotation-induced Coriolis force $F_c = 2m\Omega_z\dot{x}$, which is proportional to the drive direction oscillation amplitude is the only driving force in the sense direction. Denoting x_o and y_o as the drive and sense direction oscillation amplitudes respectively, it can be observed that the sense direction amplitude is proportional to the Coriolis force F_c , and thus to the drive direction oscillation amplitude. If $\omega_d = \omega_y$, then system is in resonance in the sense direction, and a high sense direction amplitude is expected due to sense direction resonance. If $\omega_d = \omega_x$, then system is in resonance in the drive direction, and a high sense direction amplitude is expected due to the increased Coriolis force F_c in the drive direction resonance. Thus, when $\omega_x \neq \omega_y$, the frequency response of the 2-DOF system has two resonant peaks, one at ω_x , and one at ω_y . When $\omega_x = \omega_y$, the frequency response of the 2-DOF system has one combined resonant peak, which will provide a much larger response amplitude due to coinciding drive and sense resonance peaks (Fig. 1.7).

1.4.5 Phase Relations and Proof-Mass Trajectory

In an ideal single-mass MEMS gyroscope, the oscillation pattern of the mass in the plane of the substrate depends on the phase difference between its drive and sense direction responses. The steady state response of the simplified 2-DOF system (2) will be a coupled harmonic oscillator of the form:

$$\begin{aligned} x(t) &= x_o \sin \omega_d t + \phi_x \\ y(t) &= y_o \sin \omega_d t + \phi_y \end{aligned} \tag{1.10}$$

where x_o and y_o are the drive and sense direction amplitudes respectively, and ϕ_x and ϕ_y are the drive and sense response phases. If the phase difference $\phi_y - \phi_x = 180^\circ$, then the steady-state trajectory is a straight line (Fig. 1.8a), which is the expected response of an ideal gyroscope. The slope of the straight line depends solely on the Coriolis force, thus the input rotation. Since y_o is proportional to the excitation Coriolis force F_c , which is also proportional to drive amplitude x_o , the slope of the straight line of oscillation does not depend on drive direction oscillation amplitude. If the phase difference $\phi_y - \phi_x \neq 180^\circ$, then the trajectory turns into an ellipse, which means y does not have its maximum where x is in its extreme points (Fig. 1.8b). Thus the oscillation pattern deviates from a straight line. The sense direction

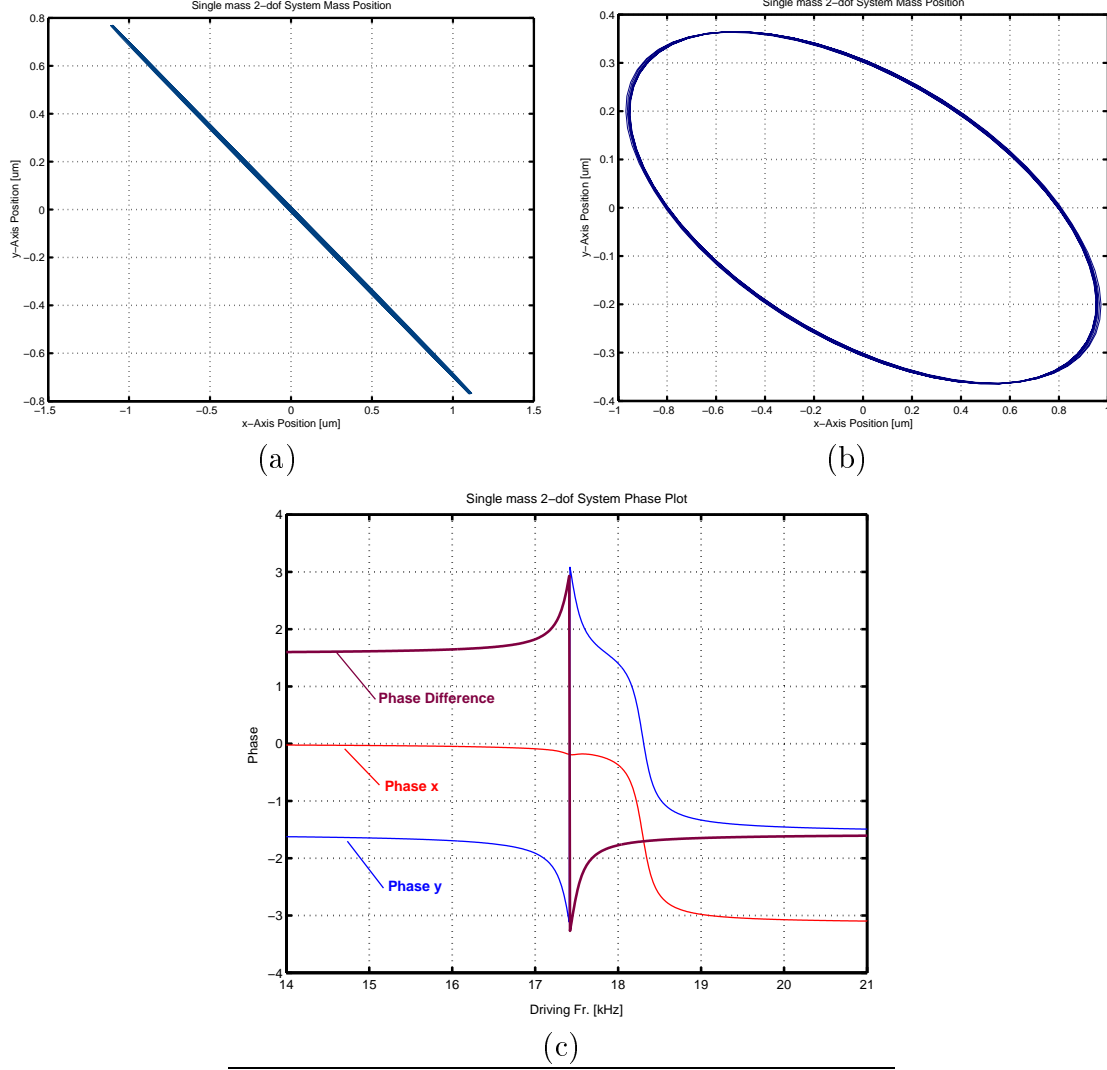


Figure 1.8: (a) The oscillation pattern when $\omega_d = \omega_y$. (b) The oscillation pattern when $\omega_d \neq \omega_y$. (c) Phase relations in x and y directions. Note that, the phase difference $\phi_y - \phi_x$ does not depend on the the drive direction resonant frequency ω_x . The phase difference is determined solely by $\omega_d - \omega_y$.

amplitude of the resulting elliptic oscillation is proportional to the Coriolis force, thus to the input rotation. However, the elliptic oscillation pattern will interfere with phase-dependent detection techniques or control forces.

When the system is driven along x -axis with a drive force of constant amplitude at the drive frequency ω_d , there will be a phase difference ϕ_x between the deflection and the force. The phase depends on the location of the driving frequency relative to the resonance peak, namely the quantity $\omega_d - \omega_x$. If $\omega_d = \omega_x$, then the system is in resonance in drive direction, and the phase difference ϕ_x between the deflection and the force is 90° (Fig. 1.8c).

Similarly, since Coriolis force F_c is the driving force in the sense direction, the deflection phase in the sense direction depends on the location of the driving frequency relative to the sense direction resonance peak, namely the quantity $\omega_d - \omega_y$. If $\omega_d = \omega_y$, then the system is in resonance in the sense direction, and the phase difference ϕ_y between the sense direction

deflection and the Coriolis force is 90° . However, it should be noticed that the Coriolis force F_c is proportional to the drive direction velocity \dot{x} , and it is always in phase with \dot{x} . Thus, F_c is always 90° phase shifted from drive direction displacement x , regardless of the driving frequency.

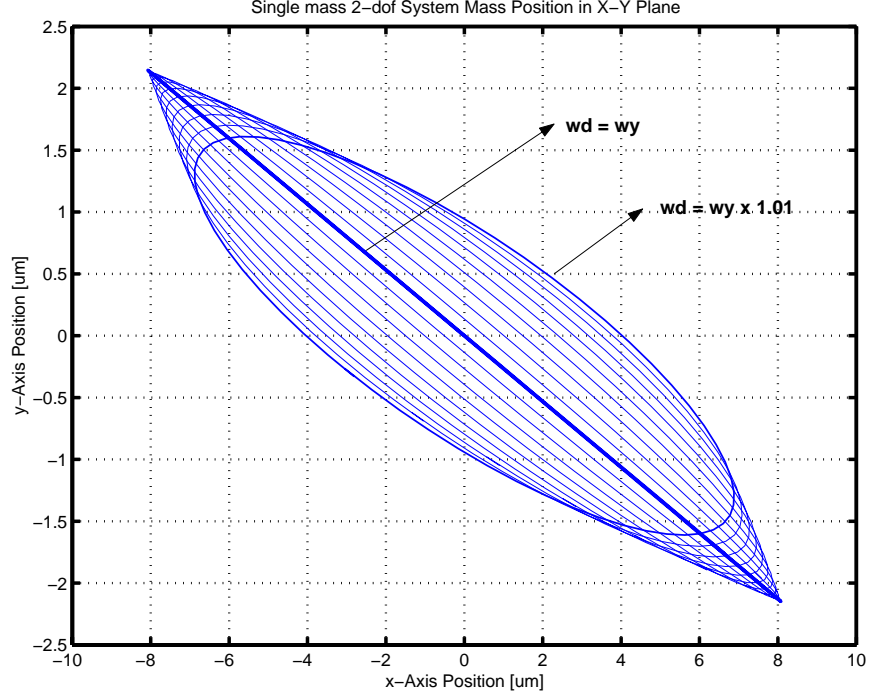


Figure 1.9: The ellipticity of the straight line of oscillation grows as the driving frequency ω_d deviates from the sense direction resonant frequency ω_y .

Consequently, phase difference between the drive and sense direction responses ($\phi_y - \phi_x$) does not depend on the location of the driving frequency with respect to ω_x . In other words, the mass trajectory is independent of $\omega_d - \omega_x$. The only frequency relation determining the trajectory is $\omega_d - \omega_y$. If $\omega_d = \omega_y$, then the drive and sense phase difference ($\phi_y - \phi_x$) is 180° because of 90° phase shift between F_c and $x(t)$, and 90° phase shift due to resonance between sense deflection $y(t)$ and the sense direction driving force F_c . Thus, when the system is driven at the sense direction resonant frequency the trajectory is a straight line. When the driving frequency ω_d deviates from ω_y , the trajectory turns into an ellipse (Fig. 1.9).

1.4.6 Anisoelasticity and Quadrature Error Issues

Fabrication imperfections and residual stresses in MEMS gyroscopes cause drive and sense direction stiffness mismatches, which result in minimum and maximum-stiffness axes in the plane of oscillation. Furthermore, the minimum and maximum-stiffness axes are likely to deviate from the drive and sense oscillation directions because of slight asymmetries in structure due to random scatter of imperfections. Due to lack of perfect alignment of the intended and

the actual principle axes of oscillation, anisoelasticity in the gyroscope structure occurs, causing dynamic cross-coupling between the drive and sense directions. The resulting dynamic cross-coupling stiffness and damping terms are the major factors that limit the performance of the gyroscope[32].

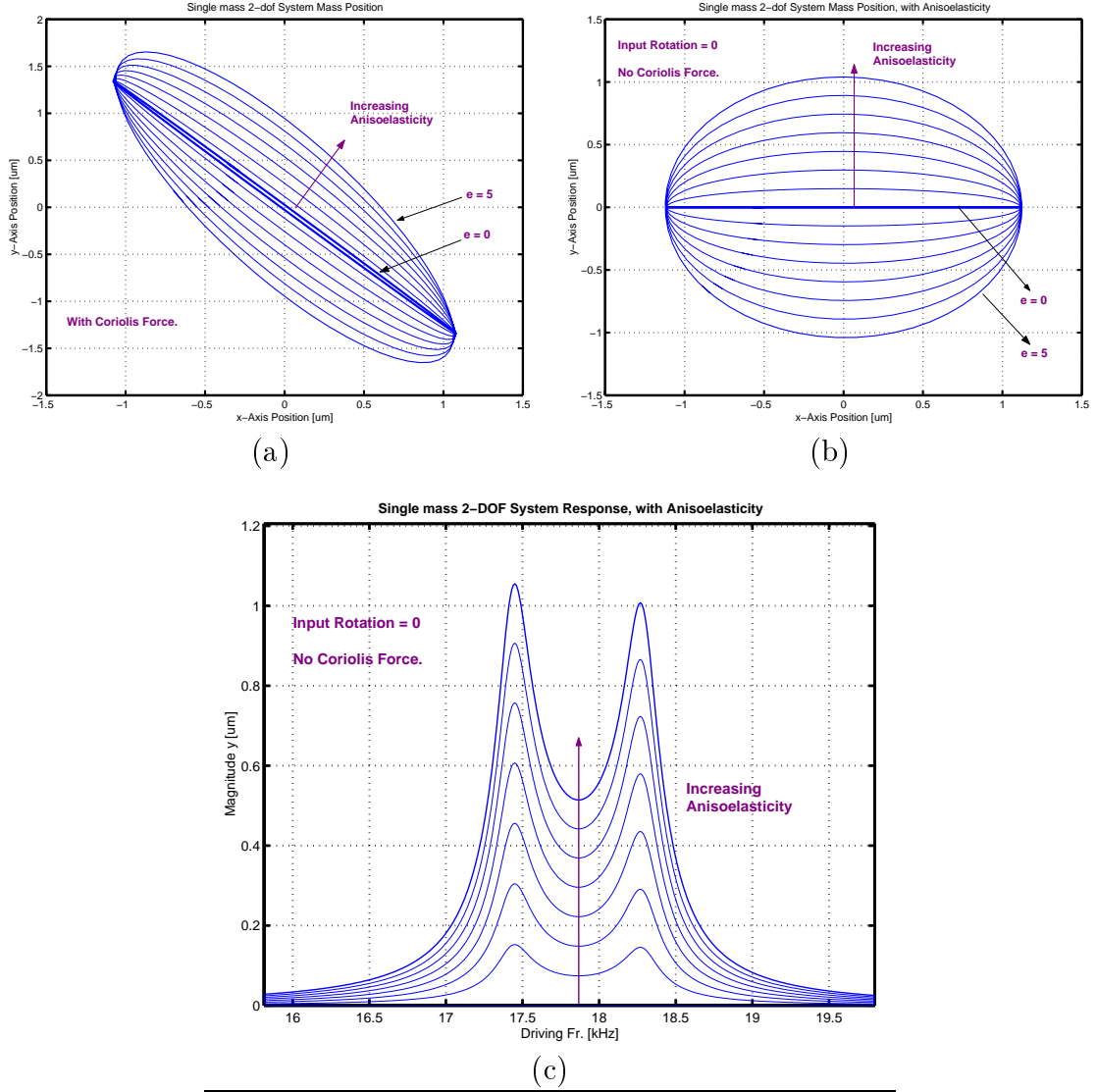


Figure 1.10: (a) Deviation of the elliptic oscillation pattern due to increasing anisoelasticity. (b) Effect of anisoelasticity on the straight line of oscillation along x -axis with zero input rotation rate. (c) In the absence of input rate, anisoelasticity induces a sense direction response similar to the Coriolis response.

Deviation of the main axes of elasticity introduces position-dependent coupling forces between the drive and sense direction transforming the straight line of oscillation to an ellipse (Fig. 1.10a). Since the coupling anisoelastic forces are in phase with the position, the resulting ellipse trajectory has a different profile than effect of x - y oscillation phase difference. It can also be observed that an angle of anisoelasticity results in the same elliptic deviation regardless of the spring constant mismatch (Fig. 1.11a), even though stiffness mismatch is

the main reason of quadrature error together with anisoelasticity. In the absence of an input angular velocity, the position-dependent anisoelastic forces cause an elliptic oscillation pattern with a response proportional to angle of anisoelasticity (Fig. 1.10b, c).

When the driving frequency is deviated from the resonant frequency of the sense direction, the mass trajectory is already an ellipse without any anisoelasticity. Furthermore, as the drive and sense phase difference $(\phi_y - \phi_x)$ deviates from 180° to 90° , the Coriolis response has the same phase as the Quadrature error, and the Coriolis signal becomes indistinguishable from the Quadrature signal if phase-related filtering techniques are used. At high quality factors, this is likely to occur with very small frequency mismatches due to the very abrupt change in phase. If anisoelasticity is introduced to the case where the oscillation is already an ellipse, the slope of the ellipse axes changes, while the drive and sense direction oscillation amplitudes vary insignificantly (Fig. 1.11b).

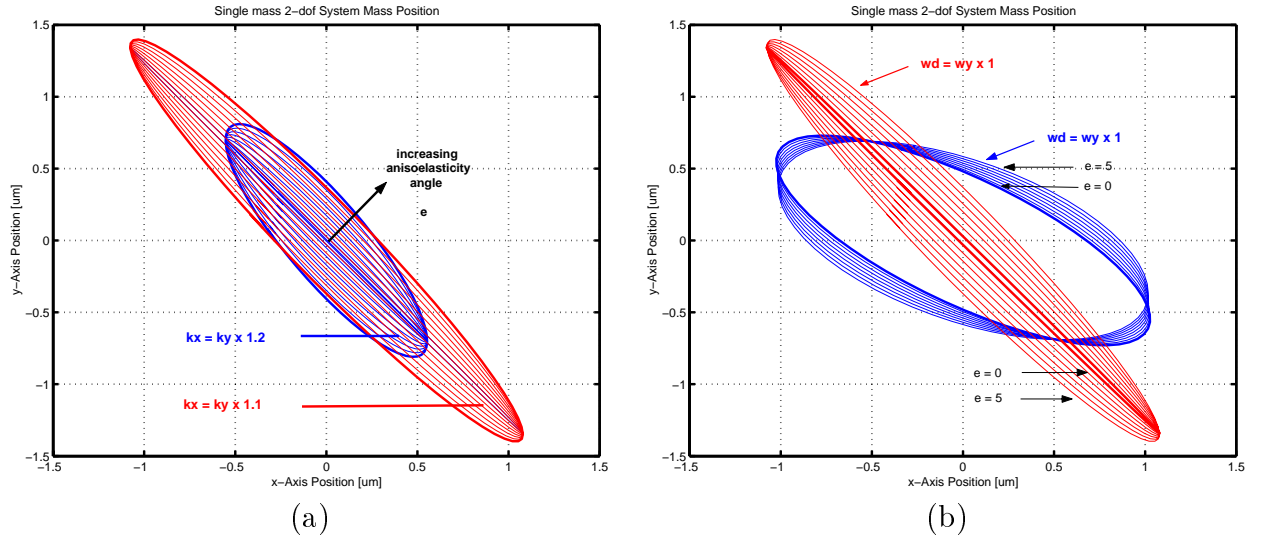


Figure 1.11: Effect of anisoelasticity on (a) stiffness mismatched systems, and (b) systems with ω_d deviated from ω_y .

1.4.7 Conclusion

In this section, the dynamics of a conventional vibratory rate gyroscope was developed, and the principle of operation of a MEMS implementation was discussed in order to highlight the limitations of the conventional approach. Consequently, all the explained factors limit the performance of the conventional gyroscopes since the system is very sensitive to variations in system parameters that shift the drive or sense resonant frequencies. Under high quality factor conditions the gain is high, however, the bandwidth is extremely narrow, which also results in abrupt phase changes. In addition, the gain and the phases are affected significantly by fluctuations in damping conditions. For proper operation of the device, these effects have to be compensated, which requires a very complicated control architecture.

Chapter 2

The 4-DOF Design Approach for MEMS Gyroscope

In this chapter, a micromachined vibratory rate gyroscope design approach that suggests the use of two independently vibrating proof masses is presented. The principle of operation is also described, and dynamics of the 4-DOF system is derived. Finally, the phase relations and mass trajectories in the ideal and non-ideal 4-DOF system are analyzed and compared to the conventional 2-DOF gyroscope systems from the sensitivity to Quadrature control point of view.

2.1 Design Approach and Principle of Operation

In contrast to the conventional micromachined gyroscopes, the proposed design approach utilizes a 4 degrees-of-freedom (DOF) dynamic system. In order to achieve dynamic amplification of mechanical motion, a system containing two mechanically coupled vibrating proof masses (Fig. 2.2) is used. The increased design parameter space allows the dynamic response of the gyroscope to be shaped as needed with much less compromise in performance. An implementation of the conceptual design, Fig. 2.1, is illustrated in Fig. 2.2.

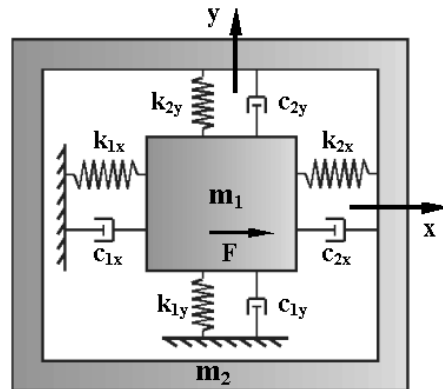


Figure 2.1: Lumped mass-spring-damper model of the dual-mass gyroscope. The first mass is driven in the x direction, and the response of the second mass along the y -axis is sensed.

2.1.1 The Design Basics

The dynamic system of the proposed micromachined gyroscope consists of the following main components: two vibrating proof masses suspended above the substrate, the flexures between the active mass and the ground that are anchored to the substrate, and the flexures between the active mass and the passive mass that mechanically couple both masses (Fig. 2.2).

The gyroscope has two orthogonal principle axes of oscillation: the drive direction (x-axis in Figure 2.1) and the sense direction (y-axis in Figure 2.1). Both of the proof masses are rendered free to oscillate in the drive and sense directions by the suspension system.

2.1.2 Principle of Operation

In the proposed design concept, the active mass (m_1 in Figure 2.1) is electrostatically forced to oscillate in the drive direction by the comb-drive structures built on each side of the mass (Fig. 2.2). There is no electrostatic force applied to the passive mass (m_2 in Figure 2.1), and the only forces acting on this mass are the elastic coupling forces and the damping forces. The design approach is based on dynamically amplifying the oscillation of the "active mass" by the "passive mass", as will be explained in Section 3.3. The response of the passive mass in the sense direction to the rotation-induced Coriolis force is monitored by the Air-Gap Sense Capacitors built around the passive mass (Fig. 2.2) providing the angular rate information.

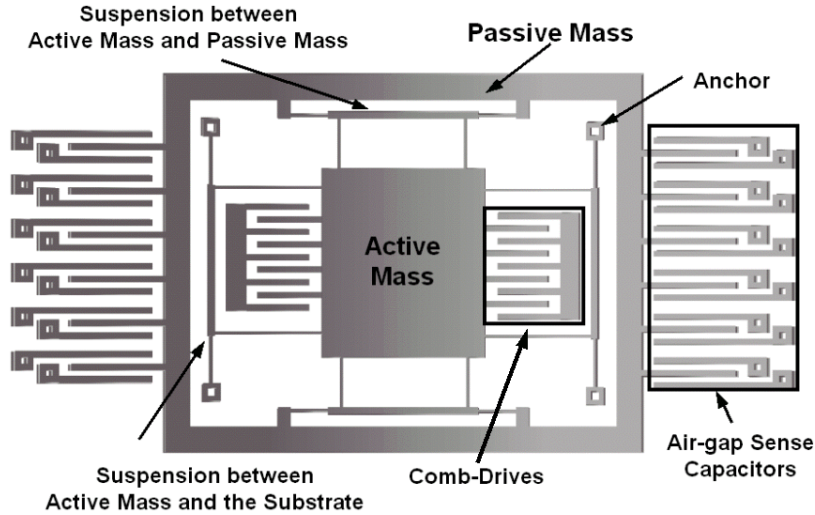


Figure 2.2: Schematic illustration of a MEMS implementation of the dual-mass z-axis gyroscope.

With appropriate selection of dynamical system parameters including the masses and the spring rates, the device will have the frequency response illustrated in Fig.2.3. There exists three regions of interest on this response curve: two resonant peaks, regions 1 and 3; and a flat region between the peaks, region 2. According to the proposed design approach, the nominal operation of the gyroscope is in the flat region, where the signal gain is relatively high, and

the sensitivity of the gain to driving frequency variations is low. Since the device is operated in the flat wide-bandwidth region, a 1% variation in natural frequencies of the system results in only 0.8% error in the output signal, whereas the same fluctuation will produce an error of 20% in the conventional micromachined gyroscopes [18].

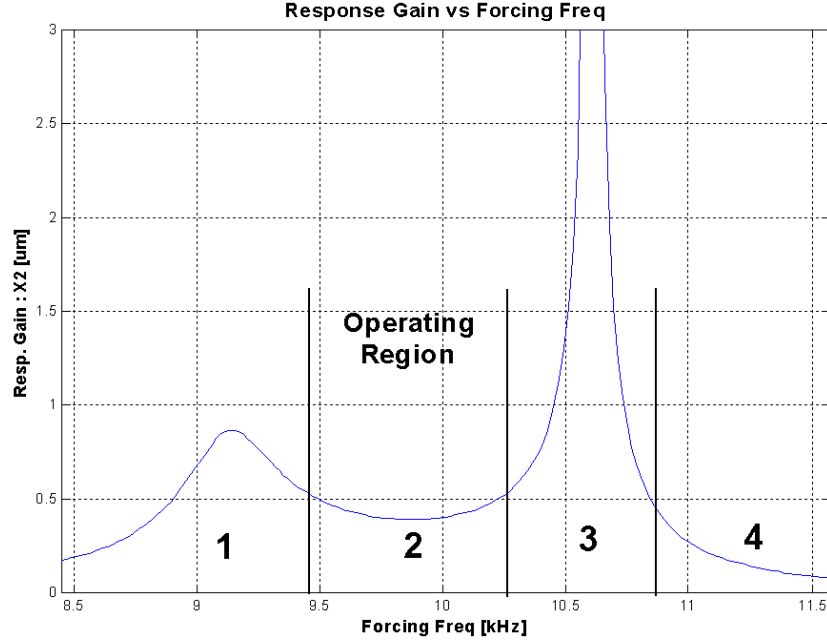


Figure 2.3: Response of the dual-mass gyroscope in the flat operation region is insensitive to resonant frequency fluctuations and has over 15 times wider bandwidth than in conventional gyroscopes.

2.2 Gyroscope Dynamics

The dynamics of the gyroscope should be considered in the non-inertial frame. Referring to Figure 2.4, the expression for absolute acceleration (in the inertial frame) of a rigid body with the position vector \vec{r} attached to a rotating reference frame B is

$$\vec{a}_A = \vec{a}_B + \vec{\Omega} \times \vec{r}_B + \vec{\Omega} \times (\vec{\Omega} \times \vec{r}_B) + 2\vec{\Omega} \times \vec{v}_B. \quad (2.1)$$

where the subscript A denotes "relative to inertial frame A ", B denotes "relative to rotating gyroscope frame B ", \vec{v}_B and \vec{a}_B are the velocity and acceleration vectors with respect to the reference frame B respectively, $\vec{\Omega}$ is the angular velocity of the gyroscope frame, and the operation " \times " refers to cross-product of two vectors. The reference rotating gyroscope frame is assumed to be non-accelerating, or linear accelerations are compensated. The last term, $2\vec{\Omega} \times \vec{v}_B$, in the equation, the Coriolis term, is of special interest since the operation of the gyroscope depends on excitation of system in the sense direction by the Coriolis force due to this term. Thus, for a mass driven into oscillation in the x-direction, and subject to an angular rate Ω_z about the z-axis, the Coriolis acceleration induced in the y-direction reduces to

$$a_y = 2\Omega_z \dot{x}(t). \quad (2.2)$$

Similarly, when the active and passive masses are observed in the non-inertial rotating frame, the "gyroscope frame", additional inertial forces appear acting on both masses. The equations of motion for the two-mass system can be written as

$$\begin{aligned} m_1 \vec{a}_1 &= F_{2-1}^{\vec{}} + F_{s-1}^{\vec{}} - 2m_1 \vec{\Omega} \times \vec{v}_1 - m_1 \vec{\Omega} \times (\vec{\Omega} \times \vec{r}_1) - m_1 \dot{\vec{\Omega}} \times \vec{r}_1 \\ m_2 \vec{a}_2 &= F_{1-2}^{\vec{}} + F_{s-2}^{\vec{}} - 2m_2 \vec{\Omega} \times \vec{v}_2 - m_2 \vec{\Omega} \times (\vec{\Omega} \times \vec{r}_2) - m_2 \dot{\vec{\Omega}} \times \vec{r}_2 \end{aligned} \quad (2.3)$$

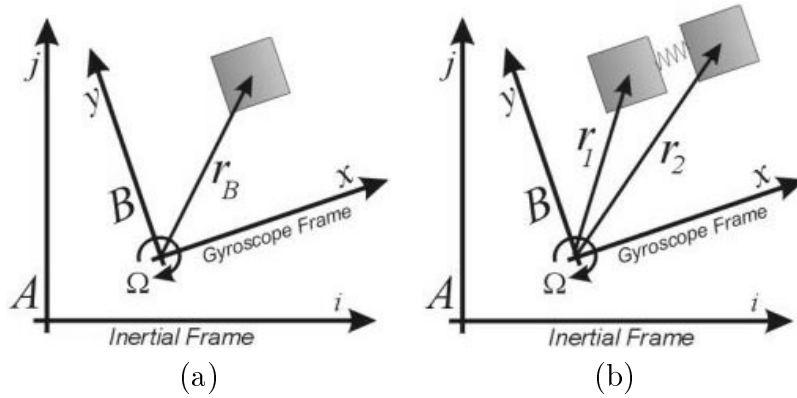


Figure 2.4: (a) Representation of the position vector of a body relative to the rotating frame. (b) Representation of the position vectors of the proof masses of the gyroscope relative to the rotating "gyroscope frame" B.

where \vec{r}_1 and \vec{r}_2 are the position vectors, \vec{v}_1 and \vec{v}_2 are the velocity vectors of the masses defined in the gyroscope frame, $F_{2-1}^{\vec{}}$ and $F_{1-2}^{\vec{}}$ are the opposing coupling forces between the masses that each mass applies on other depending on relative position $\vec{r}_2 - \vec{r}_1$, including spring and damping forces. $F_{s-1}^{\vec{}}$ consists of spring and damping forces between the active mass and the substrate, and $F_{s-2}^{\vec{}}$ includes the damping force between the passive mass and the substrate. Since both masses are subject to an angular rate of Ω_z about the axis normal to the plane of operation (z-axis), the equations of motion along the x-axis and y-axis become

$$\begin{aligned} m_1 \ddot{x}_1 + c_{1x} \dot{x}_1 + k_{1x} x_1 &= k_{2x} (x_2 - x_1) + c_{2x} (\dot{x}_2 - \dot{x}_1) + m_1 \Omega^2 x_1 - 2m_1 \Omega \dot{y}_1 - m_1 \dot{\Omega} y_1 + F_d(t) \\ m_2 \ddot{x}_2 + c_{2x} (\dot{x}_2 - \dot{x}_1) + k_{2x} (x_2 - x_1) &= m_2 \Omega^2 x_2 - 2m_2 \Omega \dot{y}_2 - m_2 \dot{\Omega} y_2 \\ m_1 \ddot{y}_1 + c_{1y} \dot{y}_1 + k_{1y} y_1 &= k_{2y} (y_2 - y_1) + c_{2y} (\dot{y}_2 - \dot{y}_1) + m_1 \Omega^2 y_1 + 2m_1 \Omega \dot{x}_1 + m_1 \dot{\Omega} x_1 \\ m_2 \ddot{y}_2 + c_{2y} (\dot{y}_2 - \dot{y}_1) + k_{2y} (y_2 - y_1) &= m_2 \Omega^2 y_2 + 2m_2 \Omega \dot{x}_2 + m_2 \dot{\Omega} x_2. \end{aligned} \quad (2.4)$$

where $F_d(t)$ is the driving electrostatic force applied to the active mass, and Ω is the angular velocity applied to the gyroscope about the z-axis.

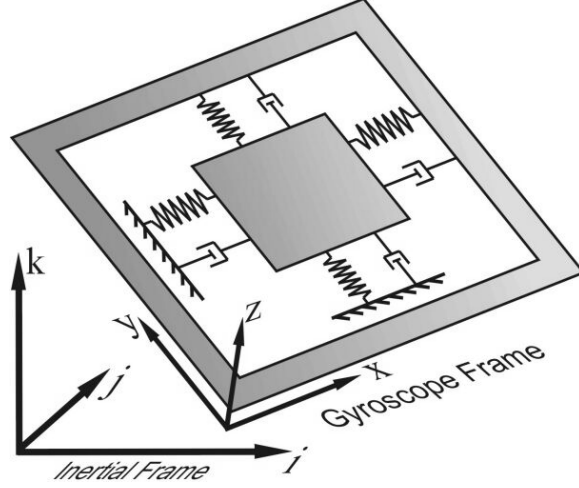


Figure 2.5: The 4-DOF dynamical system observed in the rotating gyroscope frame.

The overall dynamic model can be reduced having the active mass driven into forced oscillation in the drive direction by $F_d(t)$ with a constant amplitude x_o and a frequency ω_d . Assuming the oscillation of the first mass in the drive direction is set by the control system to be

$$x_1 = x_o \cos(\omega_d t), \quad (2.5)$$

the system (2.4) reduces to three degrees of freedom. The equations of motion of the reduced system become [18]:

$$\begin{aligned} \ddot{y}_1 + 2\omega_n \xi \dot{y}_1 + 2\mu_y \omega_n \xi (\dot{y}_1 - \dot{y}_2) + (\omega_n^2 - \Omega_z^2) y_1 + \omega_n^2 \sigma_1 (y_1 - y_2) &= -2\Omega_z \omega_d x_o \sin \omega_d t + \dot{\Omega}_z x_o \cos \omega_d t \\ \beta (\ddot{y}_2 - \Omega_z^2 y_2) + 2\mu_y \omega_n \xi (\dot{y}_2 - \dot{y}_1) - 2\beta \Omega_z \dot{x}_2 - \beta \dot{\Omega}_z x_2 + \omega_n^2 \sigma_1 (y_2 - y_1) &= 0 \\ \beta (\ddot{x}_2 - \Omega_z^2 x_2) + 2\beta \mu_x \omega_n \xi (\dot{x}_2 - \omega_d x_o \cos \omega_d t) + 2\beta \Omega_z \dot{y}_2 + \beta \dot{\Omega}_z y_2 + \omega_n^2 \sigma_2 x_2 &= w_n^2 \sigma_2 x_o \cos \omega_d t \end{aligned} \quad (2.6)$$

where $\beta = m_2/m_1$, $\sigma_1 = k_{2y}/k_{1y}$, $\sigma_2 = k_{2x}/k_{1x}$, $\mu_y = c_{2y}/c_{1y}$, $\mu_x = c_{2x}/c_{1x}$, $\xi = c_1/(2m_1 w_n)$, and $w_n = \sqrt{k_{1y}/m_1}$ is the natural frequency of the isolated active mass-spring system in the sense direction. Proper selection of system parameters including the masses m_1 and m_2 , the spring constants k_{1x} , k_{1y} , k_{2x} , and k_{2y} will result in the frequency response illustrated in Fig.2.3.

2.3 Phase Relations and Effects of Anisoelasticity

When the system is driven in the flat operating region near the drive direction antiresonant frequency, drive direction position of the active mass x_1 is 90° in phase with the electrostatic drive force F_d . With mechanical amplification, drive direction position of the passive mass x_2

is greater than x_1 , and is 90° in phase with x_1 . The Coriolis forces F_{c1} and F_{c2} acting on the active mass and the passive mass respectively are again proportional to the linear velocities of the masses, and thus they are 90° in phase with the related positions x_1 and x_2 , respectively. Since the amplitude of the passive mass is much greater than the active mass, the dominant force that drives the system in sense direction is F_{c2} , which is 90° in phase with x_2 . Thus, the force-position phase relation in sense direction determines the profile of the mass trajectories.

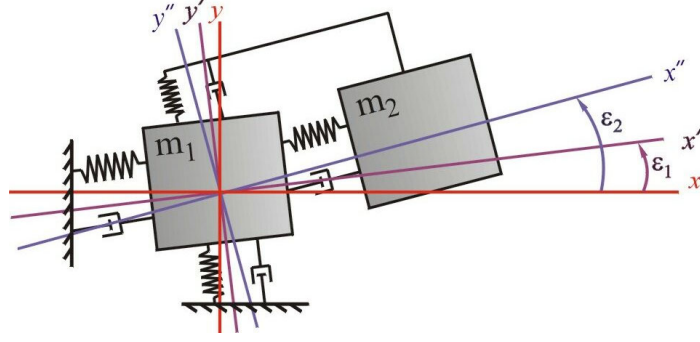


Figure 2.6: Modeling of asymmetric imperfections in the 4-DOF gyroscope. The asymmetric imperfections can be modeled as an angle of elasticity ε_1 for substrate-active mass suspension, and ε_2 for active mass-passive mass suspension.

Since the fabrication imperfection scatter is not symmetrical, the drive and sense axes in the gyroscope will not perfectly coincide with the principle axes of elasticity of the two suspension systems, which are the flexures between the active mass and the substrate, and flexures between the passive and active masses. The asymmetric imperfections can be modeled as an angle of elasticity ε_1 for substrate-active mass suspension, and ε_2 for active mass-passive mass suspension (Fig. 2.6). These angles will result in cross-coupling stiffness terms k_{1xy} and k_{2xy} , and the stiffness terms k_{1xx} , k_{2xx} , k_{1yy} , and k_{2yy} due to stiffness deviation from nominal design values.

$$\begin{aligned} k_{1xx} &= \frac{k_{1x} + k_{1y}}{2} + \frac{k_{1x} - k_{1y}}{2} \cos(2\varepsilon_1) & k_{1yy} &= \frac{k_{1x} + k_{1y}}{2} - \frac{k_{1x} - k_{1y}}{2} \cos(2\varepsilon_1) & k_{1xy} &= \frac{k_{1x} - k_{1y}}{2} \sin(2\varepsilon_1) \\ k_{2xx} &= \frac{k_{2x} + k_{2y}}{2} + \frac{k_{2x} - k_{2y}}{2} \cos(2\varepsilon_2) & k_{2yy} &= \frac{k_{2x} + k_{2y}}{2} - \frac{k_{2x} - k_{2y}}{2} \cos(2\varepsilon_2) & k_{2xy} &= \frac{k_{2x} - k_{2y}}{2} \sin(2\varepsilon_2) \end{aligned} \quad (2.7)$$

With the deviated stiffness values and the cross-coupling terms, the most general equation of motion for the non-ideal 4-DOF system can be expressed as:

$$\begin{aligned} m_1 \ddot{x}_1 + c_{1x} \dot{x}_1 + c_{2x} (\dot{x}_1 - \dot{x}_2) + k_{1xx} x_1 + k_{2xx} (x_1 - x_2) &= k_{1xy} y_1 - 2m_1 \Omega_z \dot{y}_1 + F_d(t) \\ m_2 \ddot{x}_2 + c_{2x} (\dot{x}_2 - \dot{x}_1) + k_{2xx} (x_2 - x_1) &= k_{2xy} y_2 - 2m_2 \Omega_z \dot{y}_2 \\ m_1 \ddot{y}_1 + c_{1y} \dot{y}_1 + c_{2y} (\dot{y}_1 - \dot{y}_2) + k_{1yy} y_1 + k_{2yy} (y_1 - y_2) &= k_{1xy} x_1 + 2m_1 \Omega_z \dot{x}_1 \\ m_2 \ddot{y}_2 + c_{2y} (\dot{y}_2 - \dot{y}_1) + k_{2yy} (y_2 - y_1) &= k_{2xy} y_1 + 2m_2 \Omega_z \dot{x}_2 \end{aligned} \quad (2.8)$$

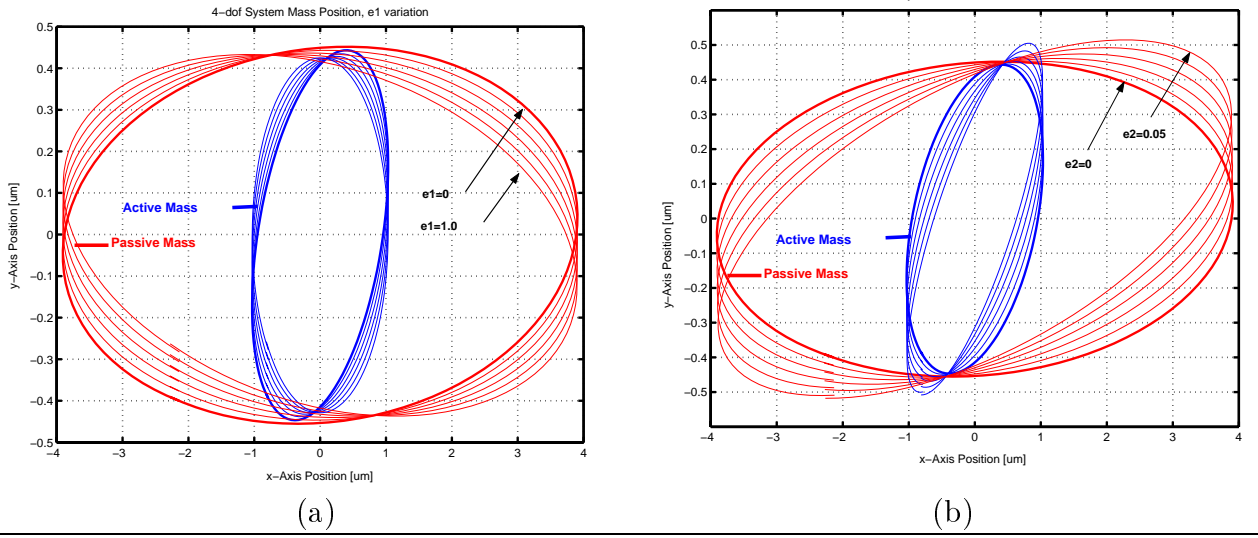


Figure 2.7: Oscillation patterns variation of the active and passive masses with (a) increasing ϵ_1 and (b) increasing ϵ_2 .

When the anisoelectricity angles ϵ_1 and ϵ_2 are introduced to the system, phase changes are observed most significantly on active mass oscillations along x -axis. Thus, anisoelectricity has the most effect on the trajectory of active mass, which is not the sensing element of the gyroscope. However, when critical values of the anisoelectricity angles ϵ_1 and ϵ_2 are exceeded, the passive mass sense amplitude increases, burying the contained Coriolis signal. It is also observed that the system is significantly immune to anisoelectricity in the active mass suspension, while the mass trajectories and gyroscope response is affected dramatically with anisoelectricity in the passive mass suspension (Fig. 2.8).

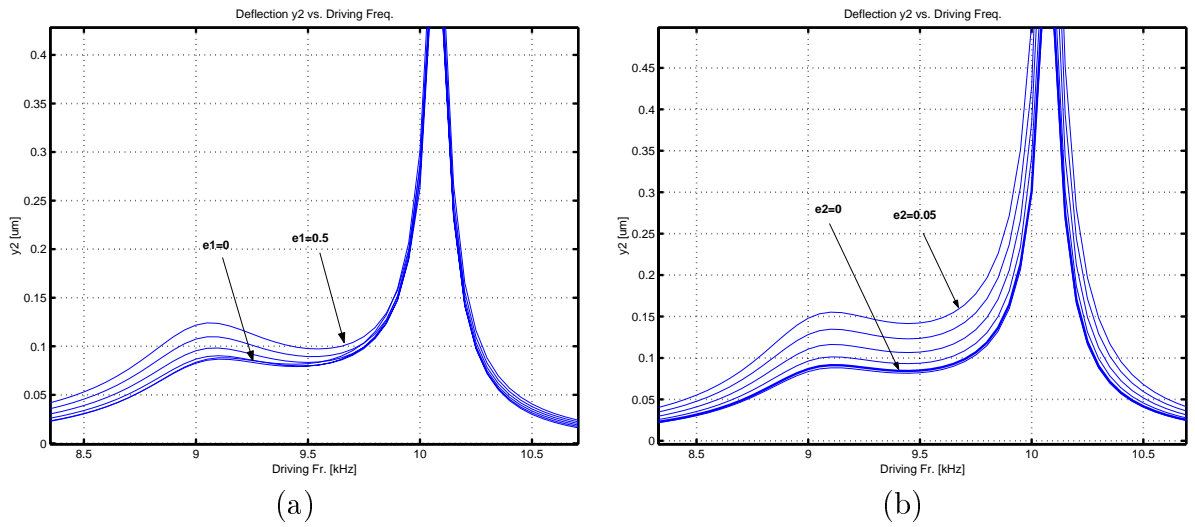


Figure 2.8: Effect of (a) ϵ_1 variation, and (b) ϵ_2 variation on 4-DOF system response.

Chapter 3

MEMS Implementation of the Design Concept

This chapter describes the principle elements of a MEMS implementation of the conceptual design presented in Chapter 2. First, the suspension system and the damping components of the dynamic system are analyzed. Then, the basics of electrostatic actuation and capacitive sensing methods are presented, followed by a detailed analysis of the drive and sense components employed in the prototype design. The issue of achieving dynamic amplification in the drive mode is addressed, and an approach for determining optimal system parameters to maximize sensor performance is presented.

3.1 Mechanical Design

In this section, the main mechanical elements of the gyroscope design, including the suspension system and the damping components, are analyzed. The theoretical models of these components are also introduced.

3.1.1 Suspension Design

The complete suspension system of the device consists of two sets of four flexible beams per each mass. For each proof mass, one set of fixed-guided beams provides the desired spring rate in the drive direction, while the other set provides the desired spring rate in the sense direction (Figure 3.1). For a single fixed-guided beam (Figure 3.2), the translational stiffness for motion in the orthogonal direction to the beam axis is given by [26]

$$k_y = \frac{1}{2} \frac{3EI}{\frac{L^3}{2}} = \frac{Et w^3}{L^3}, \quad (3.1)$$

where E is the Young's Modulus, and I is the second moment of inertia. The beam length, thickness, and width are L , t , and w , respectively.

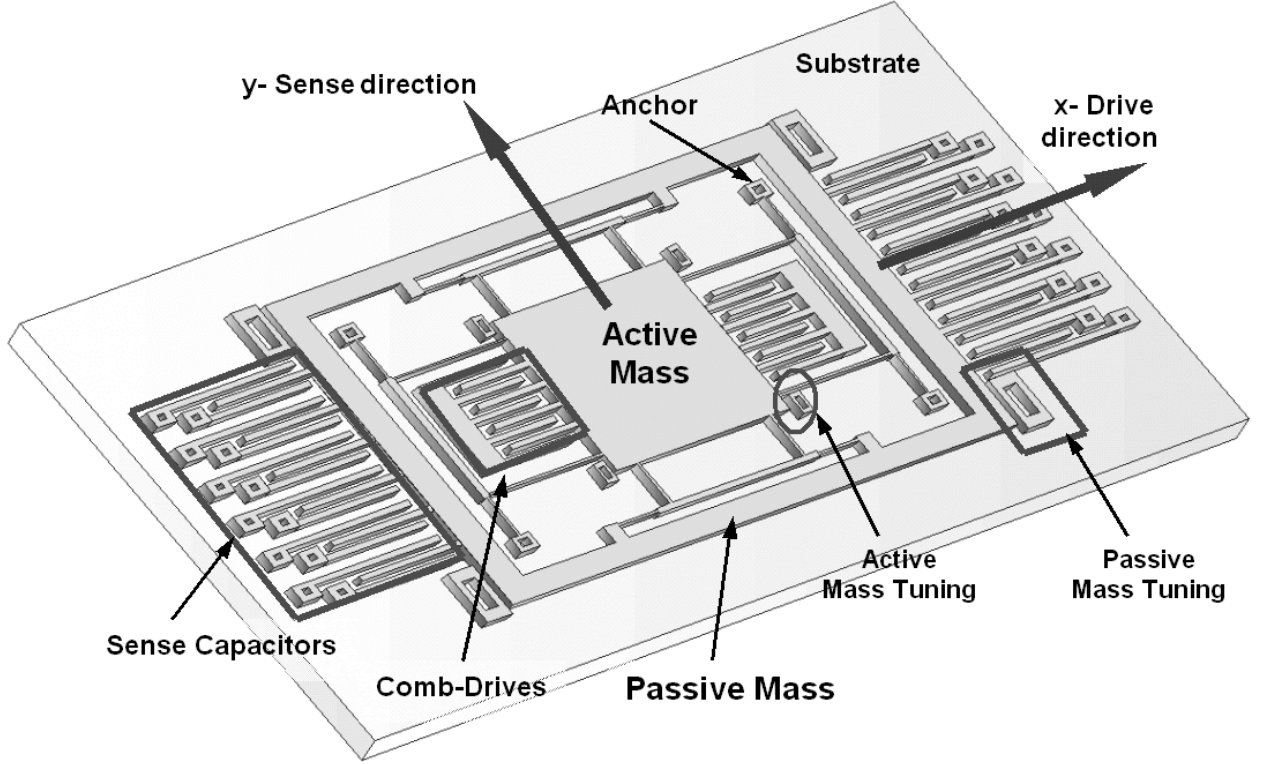


Figure 3.1: Illustration of the proposed dual-mass z-axis micromachined gyroscope design.

Spring rates for a mass in drive or sense direction are determined by four fixed-guided beams if the axial strains in the other beams are neglected. This assumption is reasonable since the axial stiffness of a beam, $k_{axial} = \frac{Etw}{L}$, is generally four orders of magnitude ($\frac{L^2}{w^2}$ times) larger than the fixed-guided stiffness, which means the beams under axial load can be assumed infinitely stiff. Each stiffness value of the suspension can be calculated as

$$k_{1x} = \frac{4Etw^3}{L_{1x}^3}, k_{1y} = \frac{4Etw^3}{L_{1y}^3}, k_{2x} = \frac{4Etw^3}{L_{2x}^3}, k_{2y} = \frac{4Etw^3}{L_{2y}^3}. \quad (3.2)$$

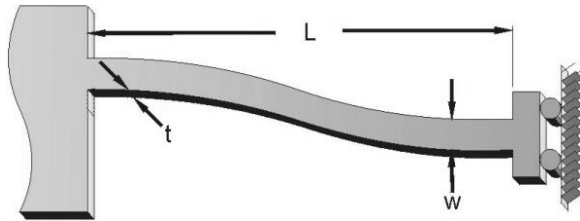


Figure 3.2: The fixed-guided end beam deflection.

where w and t are the width and thickness of the beam elements in the suspension, respectively. The individual beam lengths are shown in Figure 3.3. Finite element analysis of the gyroscope is performed using the FEA software package ANSYS to validate the assumptions in the

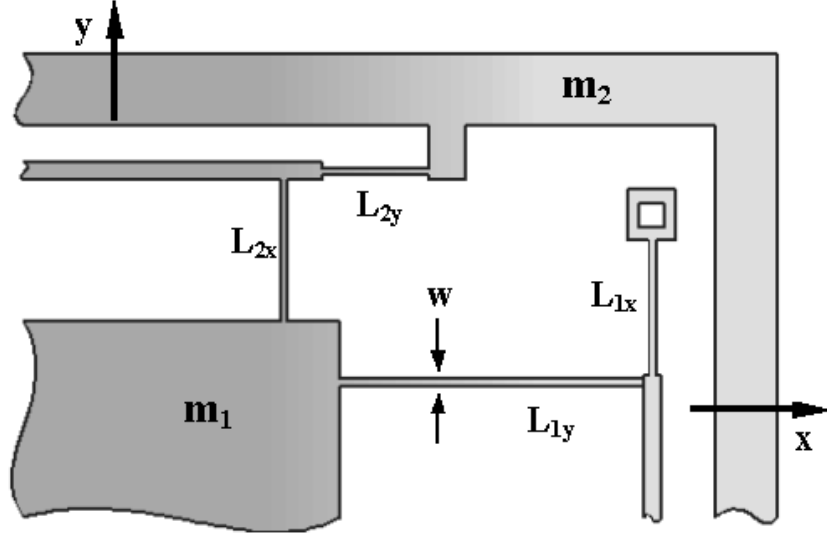


Figure 3.3: Suspension system configuration provides two degrees of freedom (in drive and sense directions) for the active proof mass and the passive proof mass.

theoretical analysis. The resonant frequencies obtained from the modal analysis matched the theoretically calculated parameters within 0.1% error. Also, it is desirable to separate the unwanted resonant modes from the operation frequency band. In FEA modal analysis, the unwanted resonant modes were also obtained, and were observed to be at least 4 kHz higher than the nominal operational frequency.

3.1.2 Damping Estimation

During the oscillation of the gyroscope proof masses, viscous effects of the air surrounding the structure results in damping. The structural damping of Polysilicon is orders of magnitude lower than the viscous damping, and is neglected in this analysis. The four damping coefficients (c_{1x} , c_{1y} , c_{2x} , and c_{2y}) in the dynamical system, shown in Figure 2.1, are due to the viscous effects of the air between the masses and the substrate, and in between the comb-drive and sense capacitor fingers. These viscous damping effects can be captured by using two general damping models: Couette flow damping and squeeze film damping.

Couette flow damping occurs when two plates of an area A , separated by a distance y_0 , slide parallel to each other (Figure 3.5). Assuming a Newtonian gas, the Couette flow damping coefficient can be approximated as:

$$c_{Couette} = \mu_p p \frac{A}{y_0}, \quad (3.3)$$

where $\mu_p = 3.710^{-4} \frac{kg}{m^2.s.torr}$ is the viscosity constant for air, p is the air pressure, A is the overlap area of the plates, y_0 is the plate separation.

Squeeze film damping occurs when two parallel plates approach each other and squeeze the

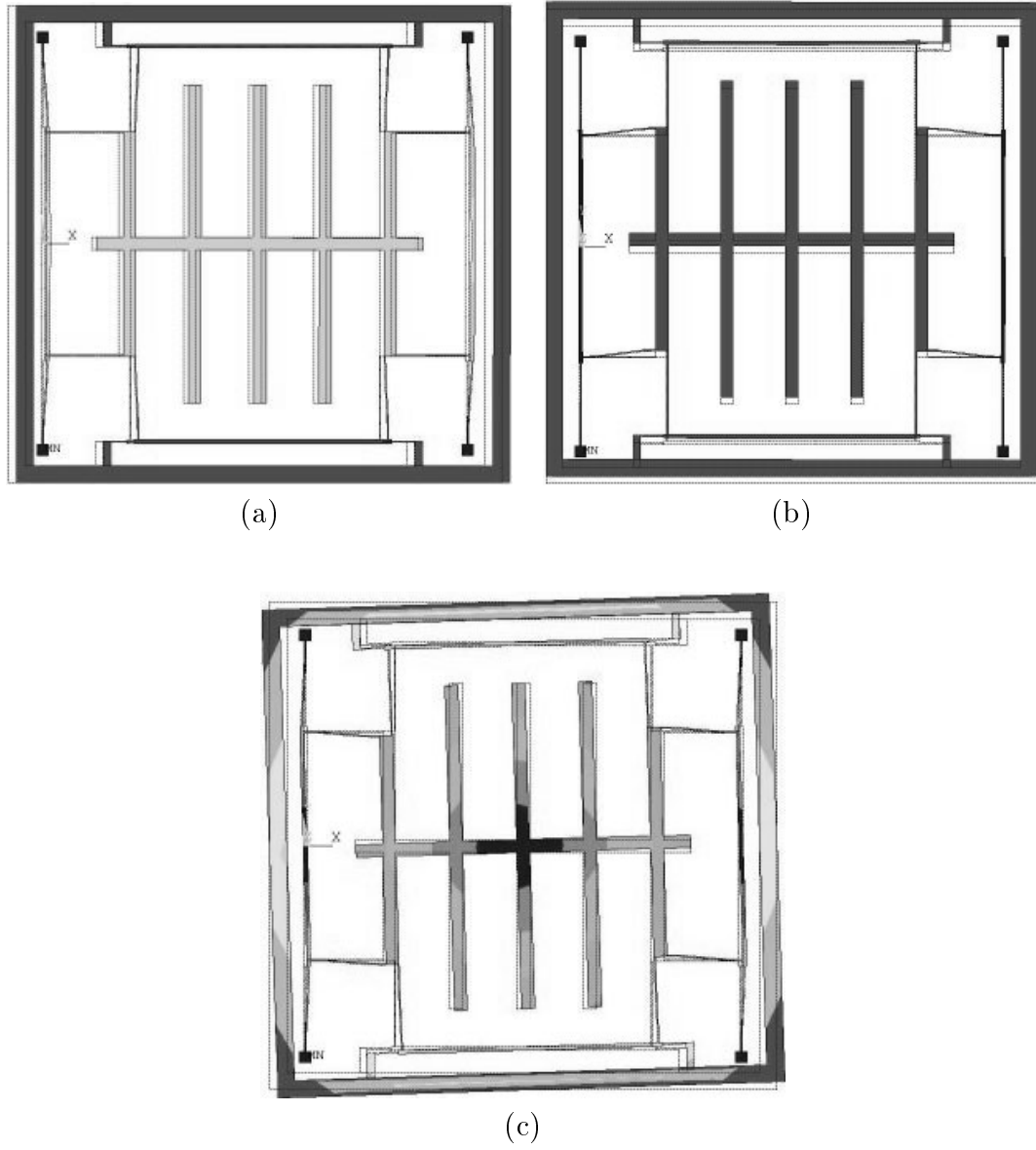


Figure 3.4: The first three resonant modes of the gyroscope. The simulation is performed using the finite element analysis package ANSYS. FEA results agree with the theoretical analysis within 0.1% error.

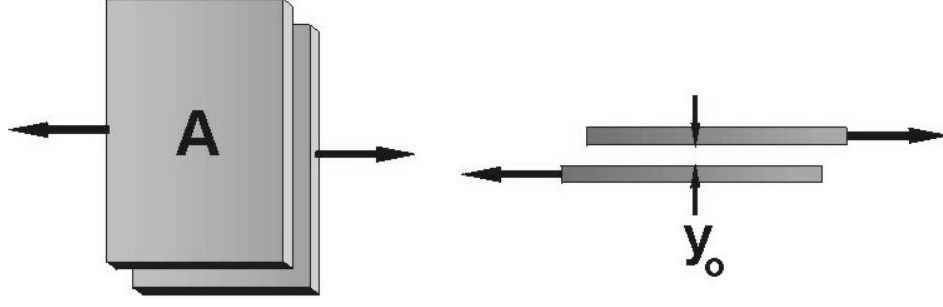


Figure 3.5: Illustration of Couette flow damping between two plates, where the plates slide along each other.

fluid film in between (Figure 3.6). Squeeze film damping effects are more complicated, and can exhibit both damping and stiffness effects depending on the compressibility of the fluid. Using the Hagen-Poiseuille law, squeeze film damping can be modeled as [28]:

$$c_{Squeeze} = \mu_p p \frac{7A z_0^2}{y_0^3}. \quad (3.4)$$

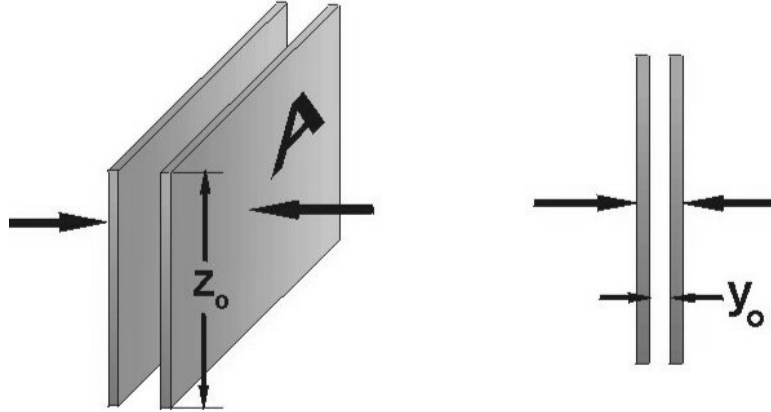


Figure 3.6: Illustration of Squeeze-film damping between two plates, where the plates move towards each other.

Utilizing the presented damping models; for the active mass, the total damping in the drive mode can be expressed as the sum of damping due to Couette flow between the mass and the substrate, and the damping due to Couette flow between the integrated comb fingers [28]:

$$c_{1x} = \mu_p p \frac{A_1}{z_0} + \mu_p p \frac{2N_{comb} l_{comb} t}{y_{comb}}, \quad (3.5)$$

where A_1 is the area of the active mass, z_0 is the elevation of the proof mass from the substrate, t is the thickness of the structure, N_{comb} is the number of comb-drive fingers, y_{comb} is the distance between the fingers, l_{comb} is the length of the fingers, p is the ambient pressure within the cavity of the packaged device, and $\mu_p = 3.710^{-4} \frac{kg}{m^2.s.torr}$ is the viscosity constant for air.

In the sense mode, the total damping is the sum of damping due to Couette flow between the proof mass and the substrate, and the Squeeze Film damping between the integrated comb fingers [28]:

$$c_{1y} = \mu_p p \frac{A_1}{z_0} + \mu_p p \frac{7N_{comb}l_{comb}t^3}{y_{comb}^3}. \quad (3.6)$$

However, for the passive mass, the total damping in the drive mode results from Couette flow between the mass and the substrate, as well as Couette flow between the air-gap capacitor fingers:

$$c_{2x} = \mu_p p \frac{A_2}{z_0} + \mu_p p \frac{2N_{capacitor}l_{finger}t}{y_{capacitor}}, \quad (3.7)$$

where A_2 is the area of the passive mass, $N_{capacitor}$ is the number of air-gap capacitors, $y_{capacitor}$ is the distance between the capacitor fingers, and $l_{capacitor}$ is the length of the fingers.

Damping of the passive mass in the sense mode can be estimated as the combination of Couette flow between the proof mass and the substrate, and the Squeeze Film damping between the air-gap capacitor fingers [28]:

$$c_{2y} = \mu_p p \frac{A_2}{z_0} + \mu_p p \frac{7N_{capacitor}l_{finger}t^3}{y_{capacitor}^3}. \quad (3.8)$$

These pressure dependent effective damping values will be used in the parametric sensitivity analysis simulations of the dynamic system.

3.2 Electrical Design

The micromachined gyroscope can be driven employing electrostatic forces, and the response can be sensed capacitively. Due to ease of manufacturing, electrostatic forcing and capacitive displacement sensing is preferred in most cases.

The electrostatic actuation and sensing components of the micromachined gyroscope can be modeled as a combination of parallel-plate capacitors (Figure 3.7). The capacitance between two parallel plates can be expressed as:

$$C = \frac{\varepsilon_0 A_{overlap}}{y_0} = \frac{\varepsilon_0 x_0 z_0}{y_0}. \quad (3.9)$$

The electrostatic force is generated due to the electrostatic conservative force field between the plates. Thus, the force can be expressed as the gradient of the potential energy U stored on the capacitor [29]:

$$\vec{F} = -\nabla U = \frac{\nabla C(x, y, z)V^2}{2} = \frac{\varepsilon_0 \nabla \left(\frac{x_0 z_0}{y_0} \right) V^2}{2} \quad (3.10)$$

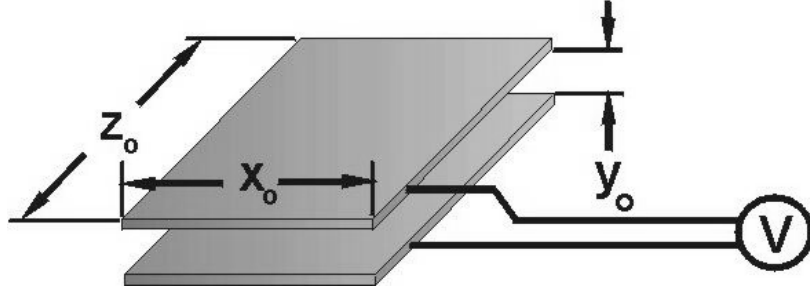


Figure 3.7: The capacitance between two plates.

The electrostatic force generated in the x -direction as parallel plates slide over each other in the x -direction can be approximated as:

$$\vec{F}_x = \frac{\varepsilon_0 V^2 z_0}{2y_0}. \quad (3.11)$$

It should be noticed that this force is independent of displacement in the x -direction and the overlapping area of the capacitor fingers. However, the electrostatic force generated in the y -direction as the plates approach to each other in the y -direction depends on the overlap area, and is a nonlinear function of displacement [27]:

$$\vec{F}_y = -\frac{\varepsilon_0 V^2 z_0 x_0}{2y_0^2}. \quad (3.12)$$

3.2.1 Electrostatic Actuation

Comb-drives are one of the most common actuation structures used in MEMS devices. The primary advantages of comb-drives (Figures 3.8a and 3.9) are the linearity of the generated forces, and the ability of applying displacement-independent forces.

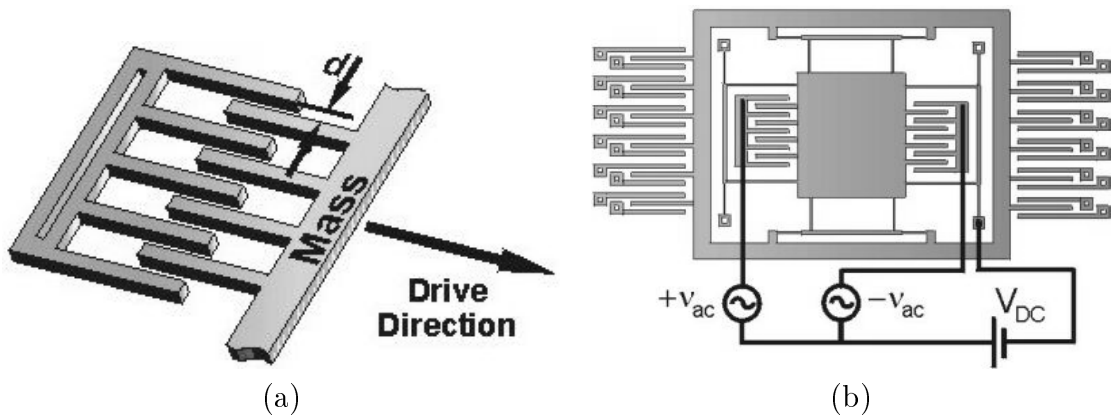


Figure 3.8: (a) The comb-drive structure for electrostatic actuation. (b) The balanced comb-drive scheme.

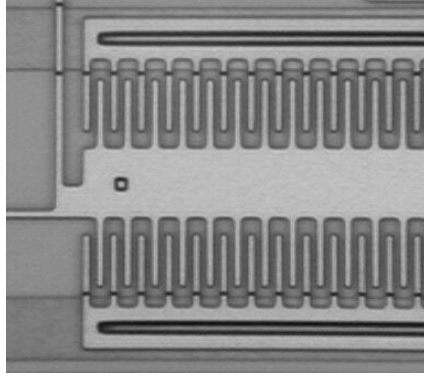


Figure 3.9: The microscope photograph of the comb-drives attached to the first mass in the fabricated prototype z-axis dual-mass gyroscope.

Linearized drive forces along the x-axis can be achieved by appropriate selection of voltages applied to the opposing comb-drive sets. A balanced interdigitated comb-drive scheme is imposed by applying $V_1 = V_{DC} + \nu_{AC}$ to one set of comb drives, and $V_2 = V_{DC} - \nu_{AC}$ to the other set (Figure 3.8b), where V_{DC} is a constant bias voltage, and ν_{AC} is a time-varying voltage. Assuming negligible deflections along the y-axis, the net electrostatic force reduces to [27]:

$$F = 4 \frac{\epsilon_0 z_0 N}{y_0} V_{DC} \nu_{AC}. \quad (3.13)$$

where z_0 is the finger thickness, and y_0 is the finger separation. It should be noticed that, the net force along the x-axis is independent of the displacement along the x-axis, and the overlap area of fingers.

3.2.2 Electrostatic Sensing

By building air-gap sense capacitors (Figures 3.10a and 3.11) around the second mass, the deflection can be capacitively sensed. When the second mass deflects in sense direction, the capacitance between the mass and the fixed electrodes changes.

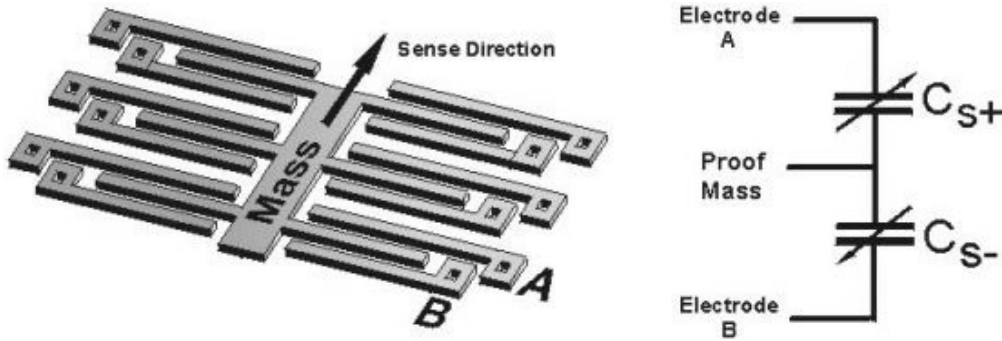


Figure 3.10: The differential air-gap sense capacitors for response sensing.

For a positive displacement, the finger attached to the mass (Figure 3.10) approaches finger A decreasing the capacitance C_{s+} , and moves away from finger B increasing the capacitance C_{s-} . The movement of the finger resulting from the deflection will translate the displacement to a change in capacitance. Defining y_0 as the finger separation, l as the length of the fingers, and t as the thickness of the fingers; the differential capacitance values can be calculated as:

$$C_{s+} = C_{s-} = N \frac{\varepsilon_0 t l}{y_0}. \quad (3.14)$$

The capacitance change should be converted into a voltage signal. The purpose of the sense electronics is to detect the small capacitance changes resulting from very small displacements of the second mass, and to provide a sufficiently high sense voltage signal.

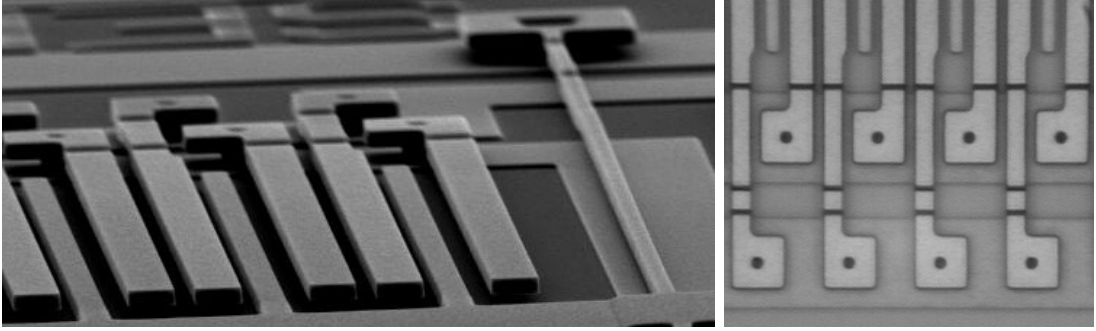


Figure 3.11: Air-gap sense capacitors attached to the second mass in the fabricated prototype z-axis dual-mass gyroscope.

3.3 Dynamic Amplification in Drive Mode

To achieve the maximum possible response of the gyroscope, amplitude of the drive-direction oscillation of the passive mass should be maximized. In the drive mode, the dynamic system is simply a 2-DOF system. A sinusoidal force is applied on the active mass by the comb-drive structure. Assuming a lumped parameter model, the equations of motion in the drive mode become:

$$\begin{aligned} m_1 \ddot{x}_1 + c_1 \dot{x}_1 + (k_1 + k_2)x_1 &= F + k_2 x_2 \\ m_2 \ddot{x}_2 + c_2 \dot{x}_2 + k_2 x_2 &= k_2 x_1. \end{aligned} \quad (3.15)$$

When a sinusoidal force $F = F_0 \sin(\omega t)$ is applied on the active mass by the interdigitated comb-drives, the steady-state response of the 2-DOF system will be

$$\begin{aligned} X_1 &= \frac{F_0}{k_1} \frac{1 - (\frac{\omega}{\omega_2})^2 + j\omega \frac{c_2}{k_2}}{[1 + \frac{k_2}{k_1} - (\frac{\omega}{\omega_1})^2 + j\omega \frac{c_1}{k_1}][1 - (\frac{\omega}{\omega_2})^2 + j\omega \frac{c_2}{k_2}] - \frac{k_2}{k_1}} \\ X_2 &= \frac{F_0}{k_1} \frac{1}{[1 + \frac{k_2}{k_1} - (\frac{\omega}{\omega_1})^2 + j\omega \frac{c_1}{k_1}][1 - (\frac{\omega}{\omega_2})^2 + j\omega \frac{c_2}{k_2}] - \frac{k_2}{k_1}}, \end{aligned} \quad (3.16)$$

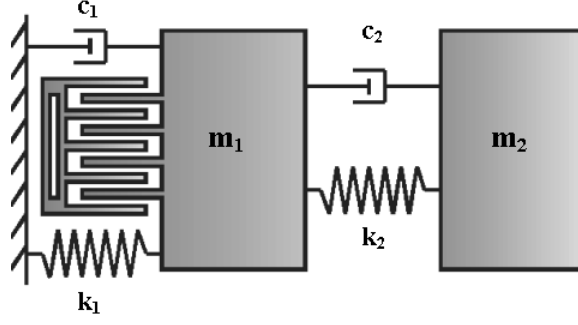


Figure 3.12: Lumped model of the drive mode of dual-mass gyroscope. The passive mass (m_2) amplifies the motion of the active mass (m_1).

where $\omega_1 = \sqrt{\frac{k_1}{m_1}}$ and $\omega_2 = \sqrt{\frac{k_2}{m_2}}$ are the resonant frequencies of the isolated active and passive mass-spring systems, respectively. When the driving frequency ω_{drive} is matched with the resonant frequency of the isolated passive mass-spring system, i.e. $\omega_{drive} = \sqrt{\frac{k_2}{m_2}}$, the passive mass moves to exactly cancel out the input force F applied to the active mass, and maximum dynamic amplification is achieved [10].

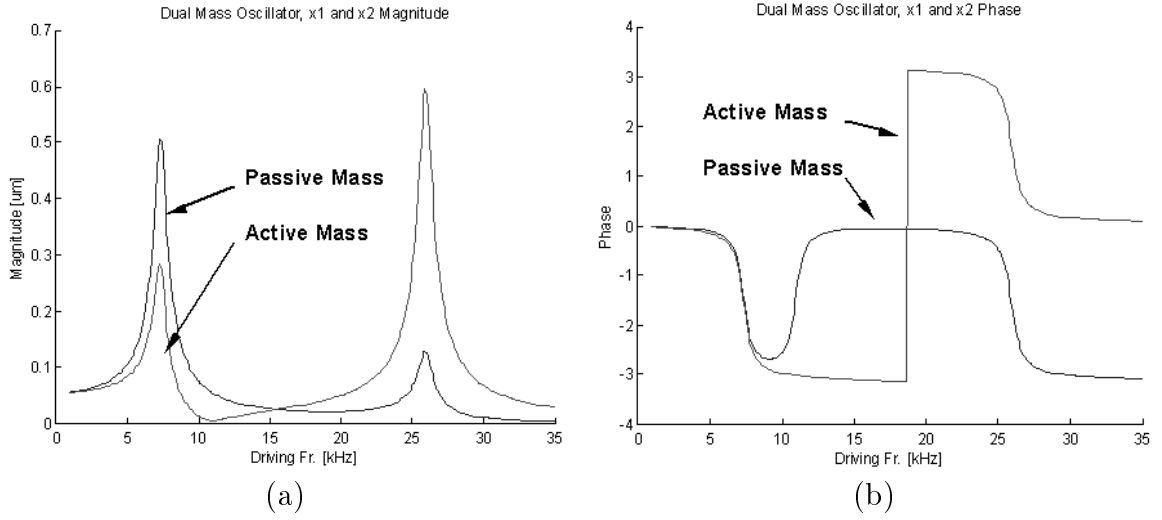


Figure 3.13: (a) The magnitude plots of each proof mass. At the antiresonant frequency, which is the resonant frequency of the isolated passive mass-spring system, oscillation amplitude of the active mass approaches to zero. (b) The phase plots of the proof masses.

The oscillation amplitudes in the drive-direction can be calculated once the magnitude of sinusoidal force $F = F_0 \sin(\omega t)$ applied to the active mass by the comb-drive structure is known. If a balanced interdigitated comb-drive scheme is utilized by applying $V_1 = V_{DC} - \nu_{AC}$ to one set of comb drives (e.g. the set on the right side in Fig. 3.8b), and $V_2 = V_{DC} + \nu_{AC}$ to the opposing set (the set on the left side); the resulting net electrostatic force is linear in ν_{AC} , which will lead to simplification of the dynamic model:

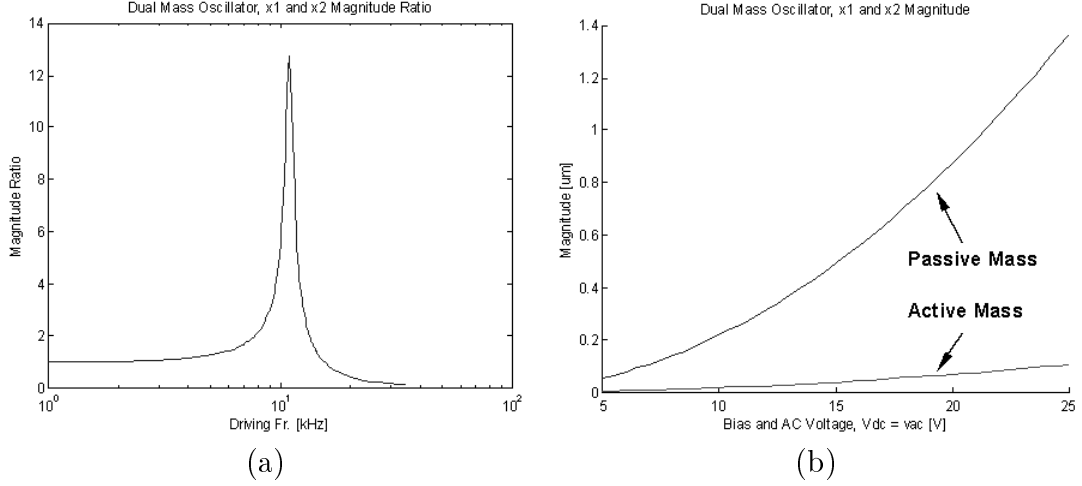


Figure 3.14: (a) The dynamic amplification ratio reaches its maximum at the antiresonant frequency, i.e., $\omega_{drive} = \sqrt{\frac{k_{2x}}{m_2}}$. (b) With a balanced interdigitated comb-drive scheme, a $1\mu m$ amplitude is achieved by the passive mass with a bias voltage of about 20V.

$$F = 4 \frac{\varepsilon_0 z_0 N}{y_0} V_{DC} \nu_{AC}, \quad (3.17)$$

where $\nu_{AC} = |\nu_{AC}| \sin \omega t$ is the sinusoidal voltage, V_{DC} is the constant bias voltage, z_0 is the finger thickness, and y_0 is the finger separation. Thus, for the gyroscope, the magnitude of the applied drive force is simply

$$F_0 = 4 \frac{\varepsilon_0 z_0 N}{y_0} V_{DC} |\nu_{AC}|. \quad (3.18)$$

assuming small oscillation amplitudes of the active mass in the sense direction, and $\nu_{AC} \ll V_{DC}$. With this balanced interdigitated comb-drive scheme, a $1\mu m$ oscillation amplitude is achieved by the passive mass in atmospheric pressure when a bias voltage of about 20V and a 5V alternating voltage is applied.

3.4 Parameter Optimization for Improved Performance

Since the foremost mechanical factor determining the performance of the gyroscope is the sense direction deflection of the passive mass due to the input rotation, the parameters of the dynamical system should be optimized to maximize the oscillation amplitude of the passive mass in the sense direction. Due to mechanical amplification in the drive mode, oscillation amplitudes of the active mass is much smaller compared to the passive mass, which generates a much smaller Coriolis Force on the active mass. Thus, the dominant force that drives the system in sense direction is the Coriolis force induced on the passive mass. This requires determining an optimal m_2 according to Coriolis Force requirement as the first step.

For a high enough Coriolis Force $2m_2\Omega_z\dot{x}_2$ acting on the passive mass, which will drive the

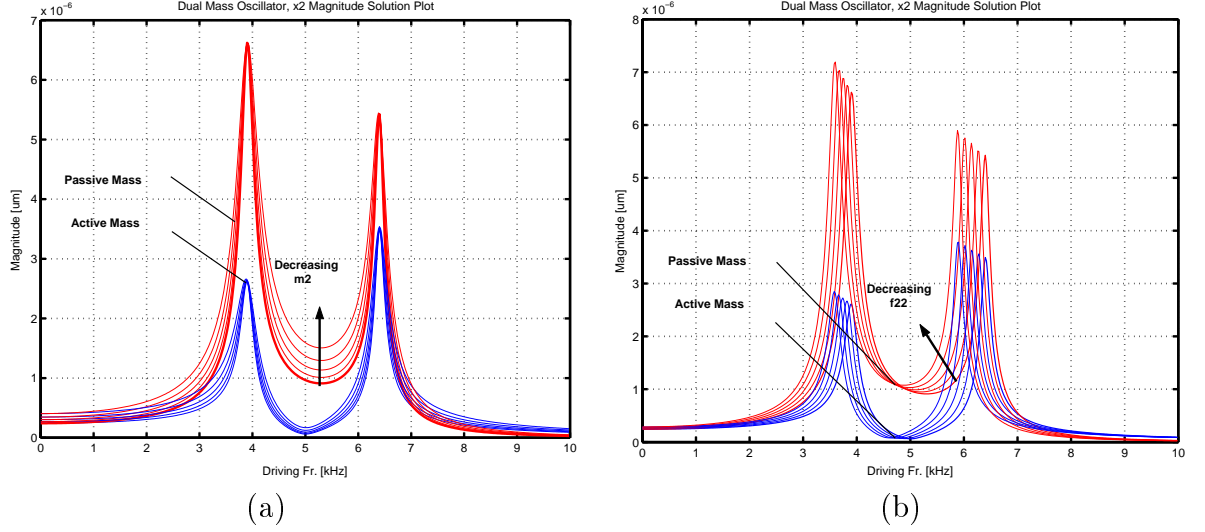


Figure 3.15: Effect of (a) passive mass m_2 variation, and (b) antiresonant frequency ω_{22} variation on drive direction response.

system in sense direction, m_2 has to be large. However, if the response of the passive mass in the drive direction is observed for varying m_2 values, it is seen that for high oscillation amplitudes of passive mass, m_2 has to be as small as possible (Fig. 3.15a). Thus, an optimal passive mass is selected based on these criteria.

As the second step, the resonant frequency ω_{22} of the isolated passive mass-spring system is determined according to gyroscope operating frequency specifications. It should be noticed that larger Coriolis forces are induced at higher frequencies, but the oscillation amplitudes become larger at lower frequencies (Fig. 3.15b). Once ω_{22} is fixed, the drive direction spring constant k_{2x} of the passive mass is obtained from ω_{22} and m_2 .

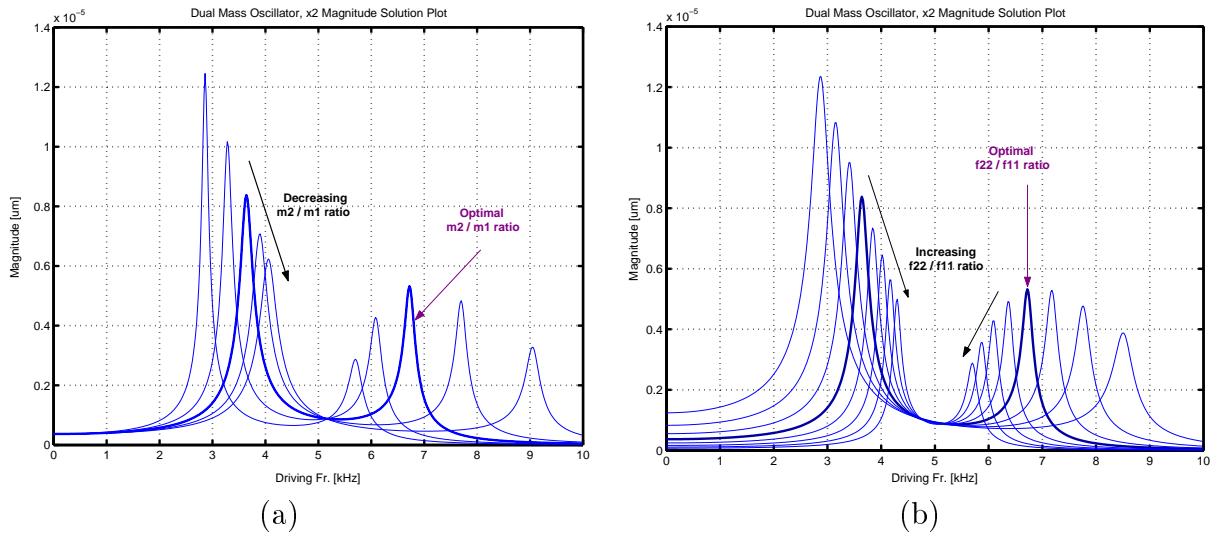


Figure 3.16: Effect of (a) mass ratio $\mu = m_2/m_1$ variation, and (b) frequency ratio $\gamma = \omega_{22}/\omega_{11}$ variation on drive direction response.

To determine the value of the active mass, an optimal mass ratio $\mu = m_2/m_1$ has to be found. In order to achieve insensitivity to damping, the resonance peaks of the 2-DOF system response have to be separated enough, which imposes a minimum value for μ . For a wide bandwidth, again a large μ is required for enough separation of the peaks; however, to prevent gain drop, the peak separation should be narrow enough (Fig. 3.16a).

The degree of mechanical amplification depends on the ratio of the isolated active and passive mass-spring systems, namely $\omega_{11} = \sqrt{k_{1x}/m_1}$ and $\omega_{22} = \sqrt{k_{2x}/m_2}$. The optimal frequency ratio $\gamma = \omega_{22}/\omega_{11}$ has to be determined such that γ is high enough for high mechanical amplification, and high oscillation amplitudes of passive mass (Fig. 3.16b). From the optimal values of ω_{11} and μ the drive direction spring constant k_{1x} of the active mass is obtained. Finally, the damping conditions of the overall device have to be checked to verify that damping values are in the region where the response gain in the antiresonance region is insensitive to damping variations (Fig. 3.17).

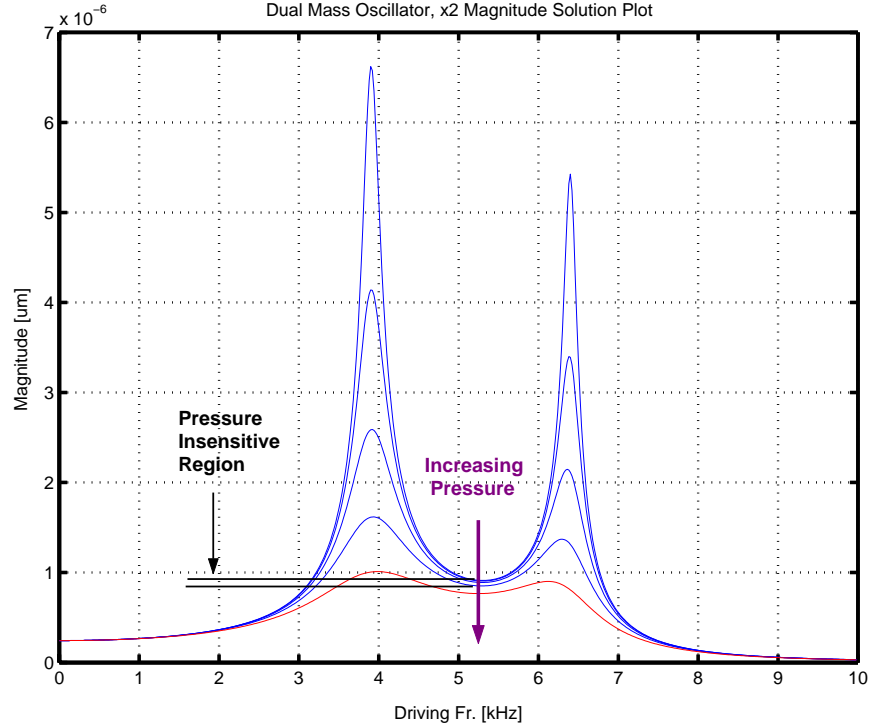


Figure 3.17: Effect of damping on drive direction response. When the damping is under a critical value, the response in the flat region is insensitive to pressure changes.

3.5 Alternative Design Implementations

Depending on the parameters of the fabrication process, the 4-DOF design concept can be implemented in various geometries. When a fabrication technology with a high structural polysilicon thickness is used, a linear design is preferred (Figure 3.1), since large actuation

forces and large sense capacitances can be achieved with the increased thickness in the comb-drives and the air-gap capacitors.

When a surface micromachining technology with a small structural layer thickness is used, a torsional design (Figure 3.18) will be more advantageous. The active mass, which is the outermost ring, will be torsionally driven about the x -axis, and its motion will be amplified by the passive mass to obtain large torsional oscillations about the x -axis. When the device is subject to an angular rate about the axis normal to the substrate, Coriolis torques will be induced on the passive mass, driving the gimbal system into torsional oscillations about the y -axis, which will be detected by the large differential parallel-plate electrodes underneath the passive mass.

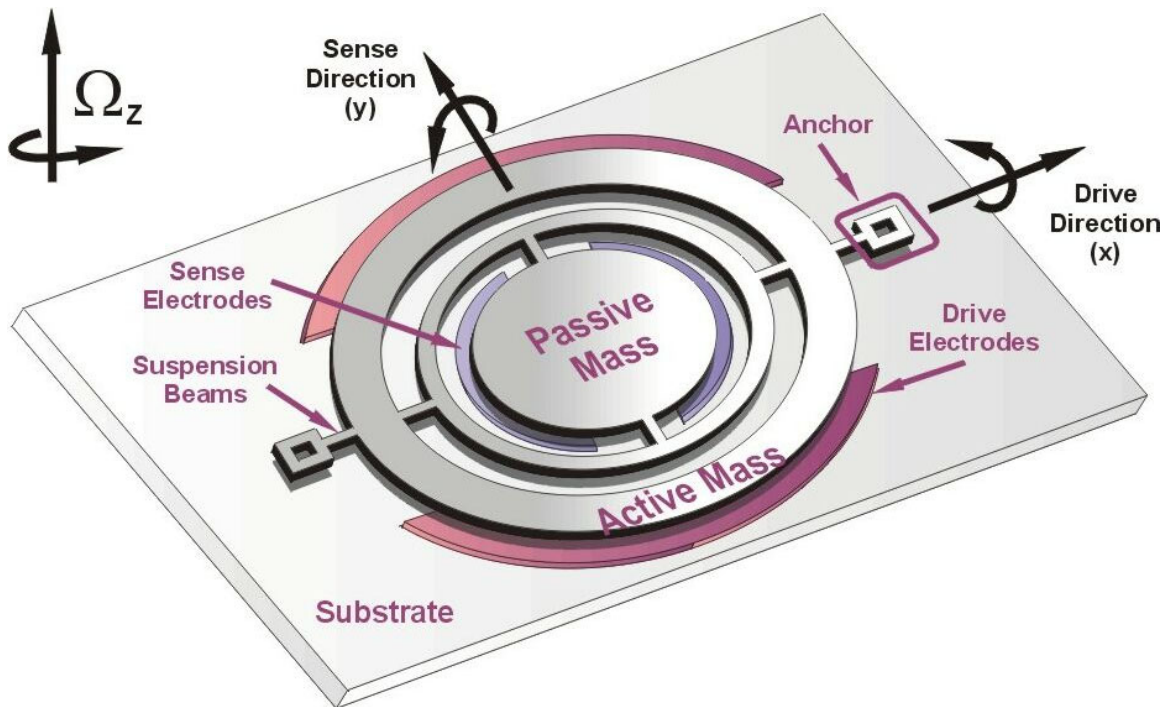


Figure 3.18: Torsional implementation of the 4-DOF design approach.

Chapter 4

Parametric Sensitivity Analysis

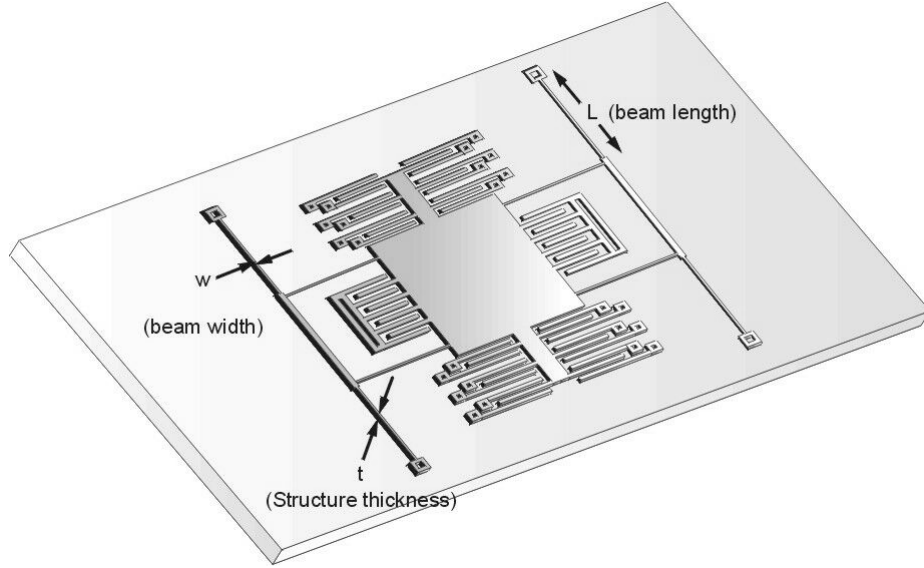
In this chapter, sensitivity analysis of the proposed micromachined gyroscope design is presented. Specifically, the sensitivity of the system response to realistic variations in system parameters are investigated, including the effects due to fabrication, pressure, and thermal variations, and residual stress. In the analysis, the robustness of the proposed system against the parameter variations is compared to a conventional design with a similar geometry.

4.1 Fabrication Variations

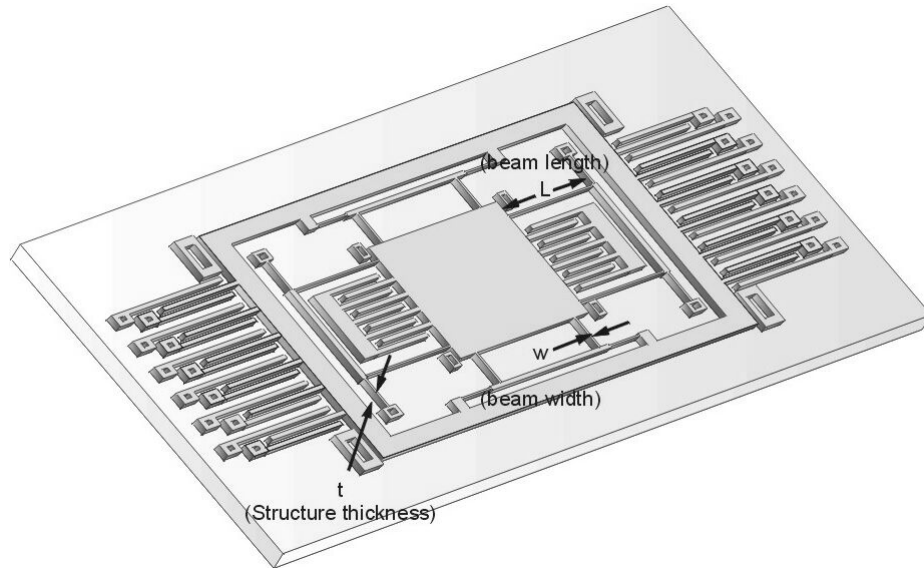
Fabrication variations affect the parameters of gyroscopes directly. For micromachining processes, the dimensions of the suspension beam elements are uncertain for different reasons. The length of the beams are determined solely by lithography, and are extremely accurate. However, the thickness is determined by deposition process, and the width set by lithography is affected by etching process. Thus, these parameters are less accurate, and can vary by 1% from wafer to wafer.

In conventional gyroscopes, fabrication variations result in resonant frequency shifts, requiring compensation by sophisticated control electronics. Yet, for the proposed system, a $0.05\ \mu m$ deviation from $2\ \mu m$ nominal beam width due to etching conditions results in less than 1% error in the gain (Fig. 4.4a). A $0.1\ \mu m$ deviation from $2\ \mu m$ nominal structure thickness due to deposition variations causes about 0.8% error in the gain (Fig. 4.4b).

Moreover, a variation in deposition conditions that affect the Young's Modulus of the gyroscopes structure by 10 GPa causes less than 0.5% error in the gain (Fig. 4.4c). The same parameter variations in a conventional micromachined gyroscope without compensation by control electronics result in over 10% error.

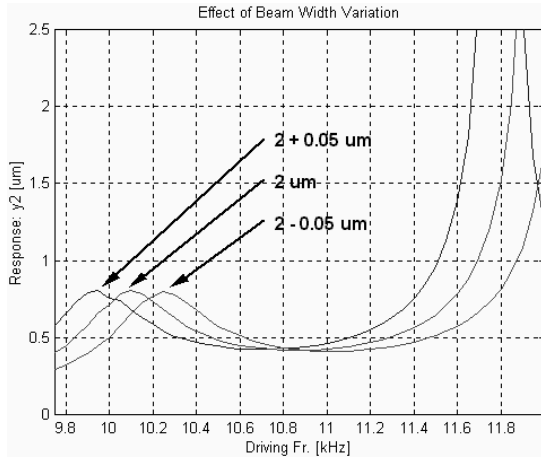


(a)

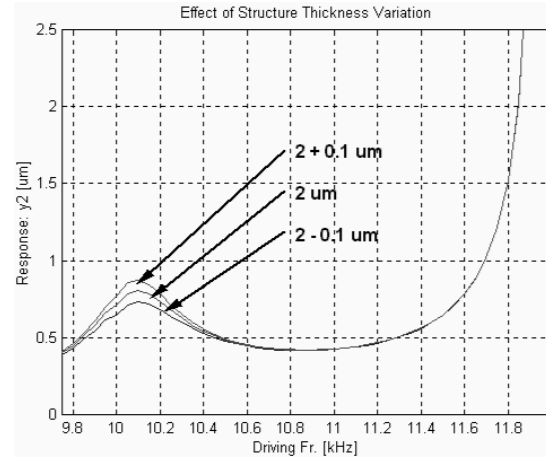


(b)

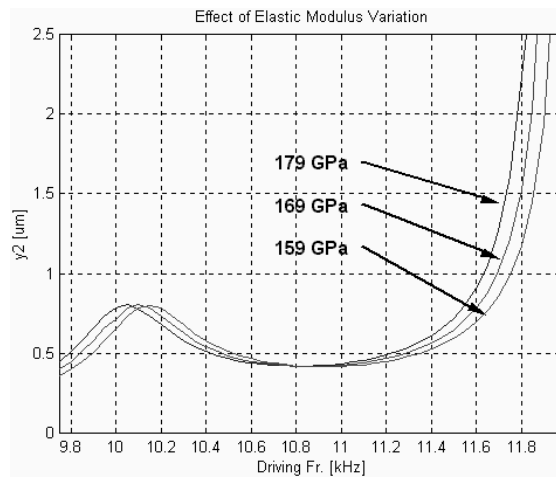
Figure 4.1: Fabrication variations can affect the geometry of the device by varying thickness of the structure or the width of the suspension beam elements. The proposed design illustrated in (b) is demonstrated to be more robust against these variations than the conventional approach illustrated in (a).



(a)



(b)



(c)

Figure 4.2: Change in the response due to: (a) $0.05 \mu\text{m}$ variation in the width of suspension beams, (b) $0.1 \mu\text{m}$ variation in thickness of the structure, (c) 10 GPa variation in Young's Modulus.

4.2 Pressure Fluctuations

Pressure fluctuations can have significant effects on resonance dependent conventional gyroscopes. In contrast, since the proposed device utilizes dynamic amplification of mechanical motion, and does not operate in resonance, the response is almost insensitive to damping changes in the operation region.

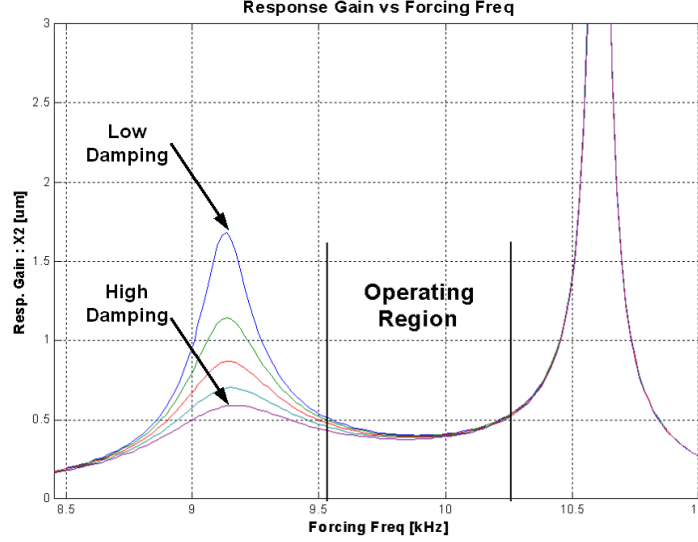


Figure 4.3: Damping changes have insignificant effect on response in the flat operation region.

For a possible vacuum leakage from 100 millitorrs to 500 millitorrs, for example due to package sealing degradation over the operation time of the device, the response gain reduces by less than 2% (Fig. 4.4a). When the effect of same pressure variation on a conventional gyroscope design is analyzed, over 60% gain reduction is observed (Fig. 4.4b).

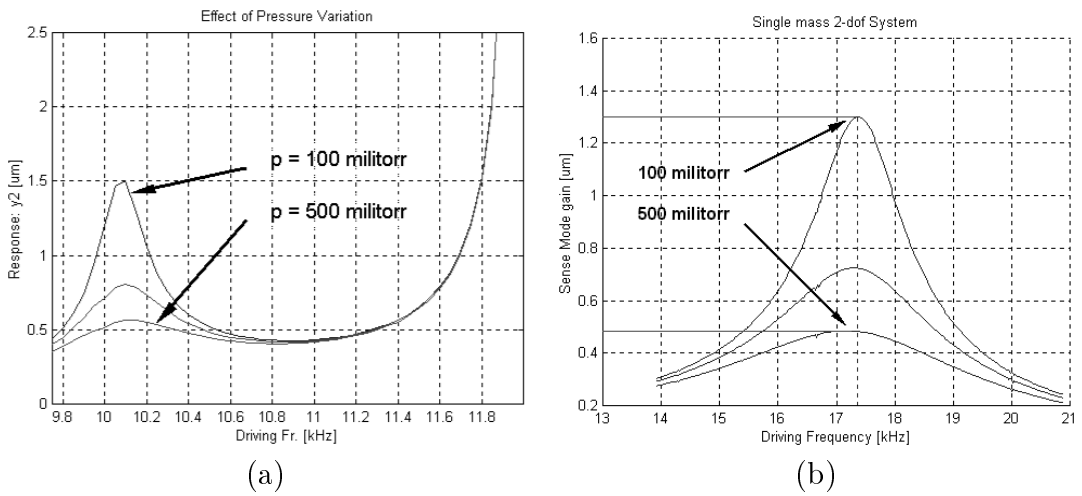


Figure 4.4: (a) Ambient pressure change from 100 millitorrs to 500 millitorrs results in 2% gain reduction for the proposed gyroscope design, (b) The same pressure change causes over 60% gain reduction for a conventional gyroscope design with similar geometry.

4.3 Thermal Fluctuations

Variations in the temperature of the structure can perturb the dynamical system parameters by three means: due to the inherent temperature dependence of Young's Modulus, due to changes in suspension geometry because of thermal expansion, and due to the thermally induced localized stress effects. Young's modulus of the structure at a given temperature can be calculated as [30]

$$E_{0^\circ C + \Delta T} = E_{0^\circ C} TC_E \Delta T + E_{0^\circ C}, \quad (4.1)$$

where $E_{0^\circ C}$ is the Young's modulus for fine-grained polysilicon at $0^\circ C$ (assumed 169 GPa), TC_E is the temperature coefficient of Young's modulus for polysilicon (assumed -75 ppm/ $^\circ C$ [30]), and ΔT is the temperature change. To reflect the effects of temperature dependent elastic modulus and thermal expansion on the resonant frequency of linear microresonators with folded-beam suspensions, the temperature coefficient of the resonance frequency can be determined as a combination of both effects [30]

$$TC_f = \frac{1}{2}(TC_E + TC_h), \quad (4.2)$$

where TC_E is the temperature coefficient of the Young's modulus, and TC_h is the temperature coefficient of thermal expansion, which is assumed 2.5 ppm/ $^\circ C$; leading to a perturbed resonant frequency of

$$\omega_{n_{0^\circ C + \Delta T}} = \omega_{n_{0^\circ C}} TC_f \Delta T + \omega_{n_{0^\circ C}}. \quad (4.3)$$

However, for the proposed suspension system, more accurate results can be found conducting finite element analysis of the system. To be able to capture parameter changes due to the temperature dependence of Young's Modulus, due to thermal expansion generated alteration in suspension geometry, and due to thermally induced stresses; a finite element model of the device was created using the finite element analysis software package ANSYS. First, a uniform temperature loading of $100^\circ C$ was applied to each surface, and the thermally induced localized stresses were observed. The results of the thermal finite element simulation indicated that a stress of 82 MPa was induced only in the drive-direction beam elements of active mass, affecting only k_{1x} . The other beam elements of the suspension system were observed stress-free (Figure 4.6a). Then, static structural analysis of the thermally loaded system with the modified Young's modulus was performed to calculate each of the four spring rates (k_{1x} , k_{1y} , k_{2x} , and k_{2y}) in the dynamical system shown in Figure 2.1. The same procedure was also carried out for a uniform temperature loading of $-100^\circ C$. The simulation of the dynamical system with the perturbed parameters due to thermal loading indicated a deviation of less than 0.9% in the gain of the gyroscope response. Finite element analysis of a conventional gyroscope with similar geometry demonstrated about 7% gain error for the same thermal loading.

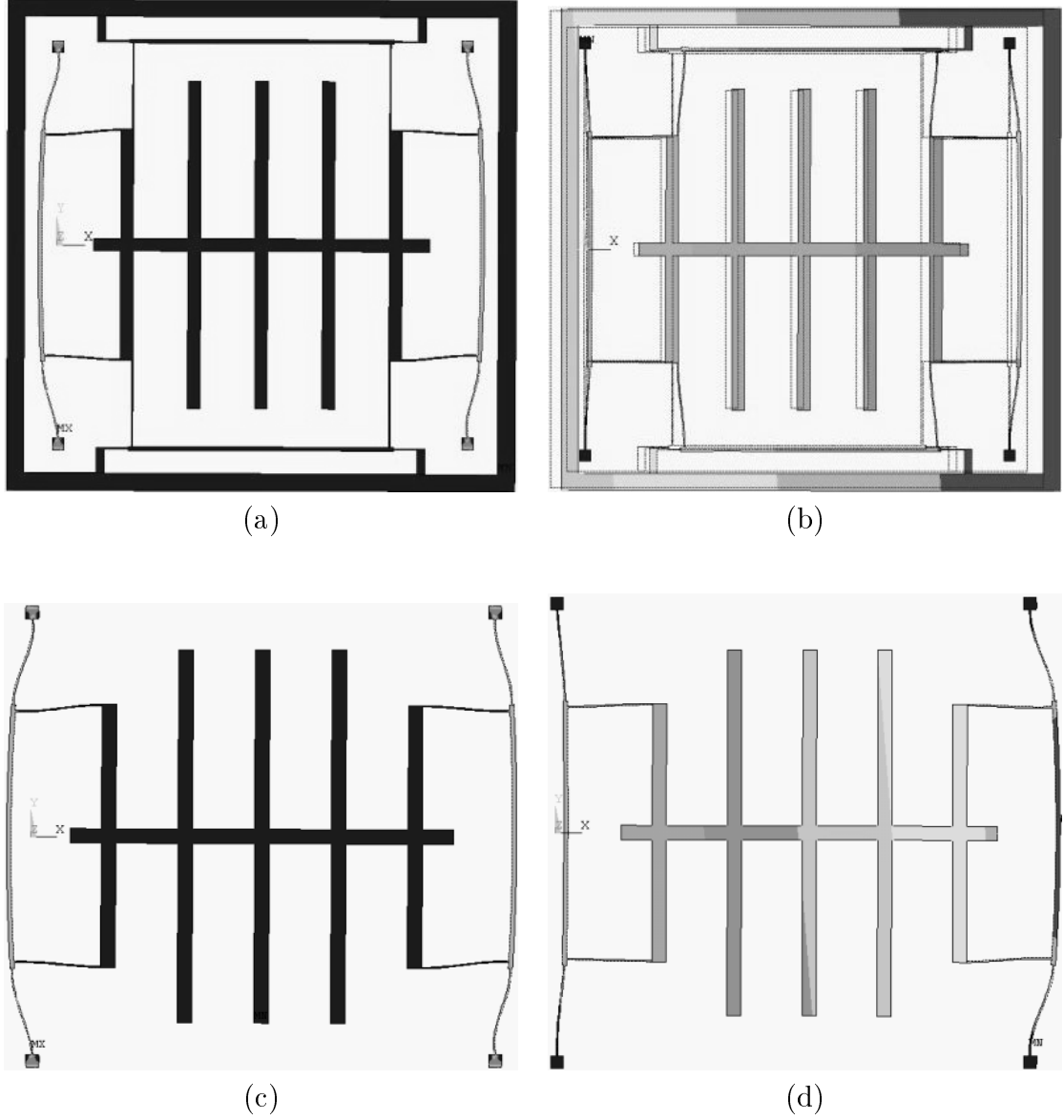


Figure 4.5: (a) Finite element simulation of the device with a uniform temperature loading of $100^{\circ}C$. Thermally induced localized stresses were observed only in the drive-direction beam elements of active mass, effecting only k_{1x} . (b) Static finite element analysis of the thermally loaded system with the modified Young's modulus. (c) Finite element analysis of a conventional gyroscope with similar geometry, under the same thermal loading. (d) Static analysis of the conventional design indicate the localized stresses leading to frequency mismatch between the drive and the sense resonant frequencies.

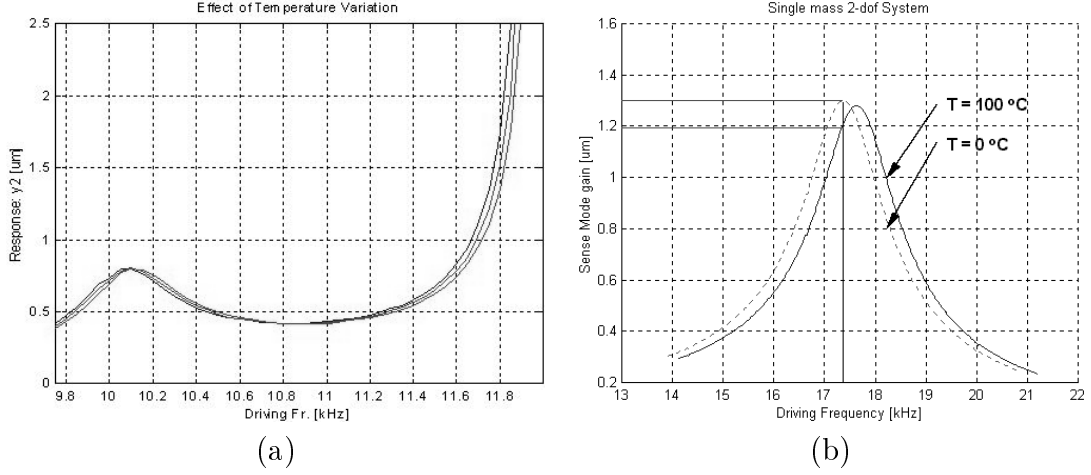


Figure 4.6: (a) Simulation of the proposed design's dynamical system with the perturbed parameters due to thermal loading, indicating less than 0.9% gain deviation. (b) Simulation of the conventional design with the perturbed parameters indicates 7% gain error for the same thermal loading.

4.4 Residual Stresses

Accumulation of residual stresses in the structure directly affect the properties of the dynamical system. In the presence of residual stresses, the beam stiffness values, and thus the overall system spring rates change. Axial residual stresses in the x-direction effect only the y-direction spring rates (k_{1y} and k_{2y}) of the suspension, while axial residual stresses in y direction effect only the x-direction spring rates (k_{1x} and k_{2x}).

Thus, for the suspension system with an x-direction axial residual stress of ε_x and a y-direction axial residual stress of ε_y , the deviation from the stress-free spring rate values become [3]

$$\Delta k_{1x} = \frac{Etw\kappa_y^2}{12L_{1x}} \left[1 - \frac{2w}{\beta_{1x}L_{1x}} \frac{\cosh\left(\frac{\kappa_y L_{1x}}{w}\right) - 1}{\sinh\left(\frac{\kappa_y L_{1x}}{w}\right)} \right]^{-1} \quad (4.4)$$

$$\Delta k_{1y} = \frac{Etw\kappa_x^2}{12L_{1y}} \left[1 - \frac{2w}{\beta_{1y}L_{1y}} \frac{\cosh\left(\frac{\kappa_x L_{1y}}{w}\right) - 1}{\sinh\left(\frac{\kappa_x L_{1y}}{w}\right)} \right]^{-1} \quad (4.5)$$

$$\Delta k_{2x} = \frac{Etw\kappa_y^2}{12L_{2x}} \left[1 - \frac{2w}{\beta_{2x}L_{2x}} \frac{\cosh\left(\frac{\kappa_y L_{2x}}{w}\right) - 1}{\sinh\left(\frac{\kappa_y L_{2x}}{w}\right)} \right]^{-1} \quad (4.6)$$

$$\Delta k_{2y} = \frac{Etw\kappa_x^2}{12L_{2y}} \left[1 - \frac{2w}{\beta_{2y}L_{2y}} \frac{\cosh\left(\frac{\kappa_x L_{2y}}{w}\right) - 1}{\sinh\left(\frac{\kappa_x L_{2y}}{w}\right)} \right]^{-1}. \quad (4.7)$$

where $\kappa_x = \sqrt{12\varepsilon_x}$, $\kappa_y = \sqrt{12\varepsilon_y}$ are the dimensionless strain factors for beam bending, and $\beta_{1x} = \frac{L_{1x}w}{\kappa_y}$, $\beta_{1y} = \frac{L_{1y}t}{\kappa_x}$, $\beta_{2x} = \frac{L_{2x}w}{\kappa_y}$, $\beta_{2y} = \frac{L_{2y}t}{\kappa_x}$.

However, an axial residual stress ε_x in the x direction effects the sense-direction spring rates (k_{1y} and k_{2y}) of the same order, and an axial residual stress ε_y in the y direction effects the drive-direction spring rates (k_{1x} and k_{2x}) of the same order as well. In result, the overall system response is less sensitive to residual stresses (Fig. 4.7). To compare the sensitivity

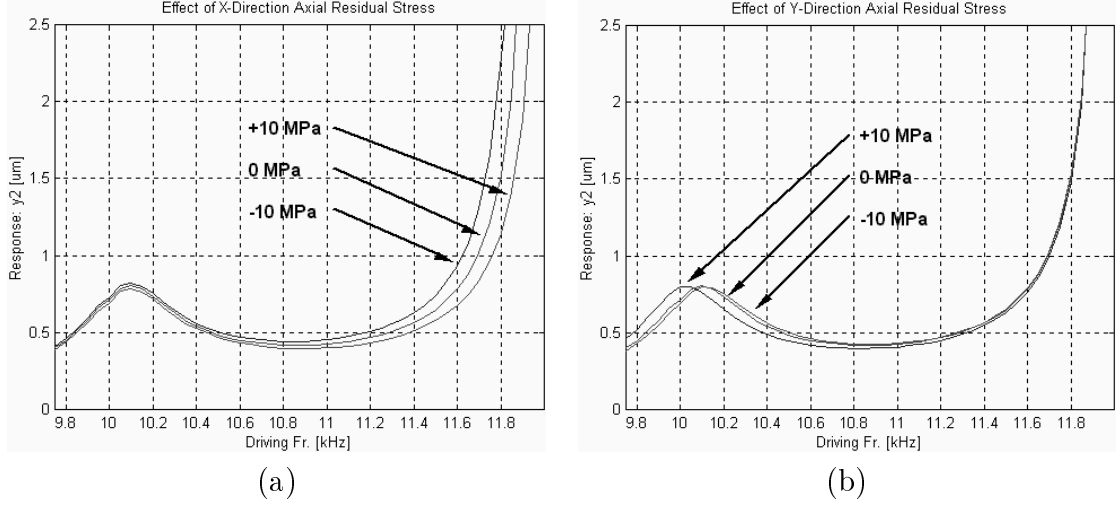


Figure 4.7: Effect of residual stresses from -10MPa to 10MPa (a) in x-direction, (b) in y-direction.

of the proposed device to the conventional approach, the designed system and a single mass gyroscope with the same geometry of the isolated active mass-spring system were simulated with a 10 MPa compression residual stress. The single-mass system experienced approximately 2.5% gain reduction, while the proposed device experienced less than 0.2% deviation in the gain.

4.5 Conclusion

In this section, sensitivity analysis of the proposed design was studied. The effects of realistic parameter variations on the system response are investigated, and the robustness of the proposed system against these variations is compared to the conventional designs. Sensitivity analysis revealed that, for the same thermal loading, the device produces 87% less error than conventional gyroscopes. Moreover, the proposed design was shown to be approximately 12 times less sensitive to residual stresses, and 20 times less sensitive to fabrication variations than conventional gyroscopes.

Chapter 5

Preliminary Experimental Results

In this chapter, fabrication of a prototype 4-DOF gyroscope is discussed along with an overview of the used fabrication technology and the experimental setup. Then, the preliminary experimental results verifying the major operational principles of the 4-DOF gyroscope are presented.

5.1 Fabrication of a Prototype

The design concept of a wide-bandwidth micromachined z-axis gyroscope can be implemented in any standard surface or bulk micromachining process. For the purpose of illustration, a design of a z-axis gyroscope implemented using two-layer $2\text{ }\mu\text{m}$ surface micromachining fabrication process is presented.

The general features of a standard two-layer surface micromachining process include utilization of polysilicon as the structural material, LPCVD deposited oxide (PSG) as the sacrificial layer, and silicon nitride as electrical isolation between the polysilicon and the substrate.

In a standard three polysilicon layer surface micromachining process, the moving parts of the device are formed using the second structural polysilicon layer (Poly1) or the third (Poly2). The electrical connections are formed using the first structural polysilicon layer (Poly0) deposited on the nitride-covered substrate [25]. Summary of the process is followed.

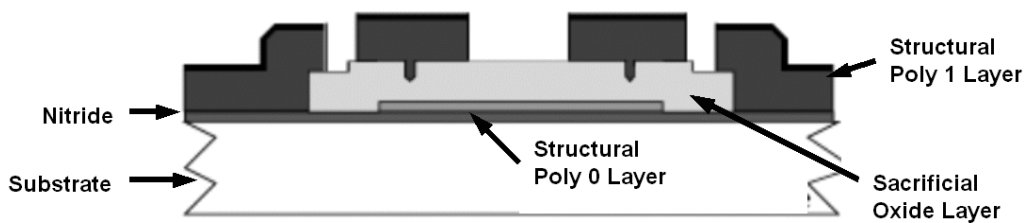


Figure 5.1: Cross-section of a device fabricated using the first two structural layers of MUMPs micromachining process [25].

5.1.1 MUMPs Surface Micromachining Process

For fabrication of a prototype of the gyroscope, commercially available Multi-User MEMS Processes (MUMPs) offered by Cronos/JDS Uniphase was used. MUMPs is a standard three-layer polysilicon surface micromachining technology. However, the prototype gyroscope structures employ only the first two structural layers, Poly0 and Poly1.

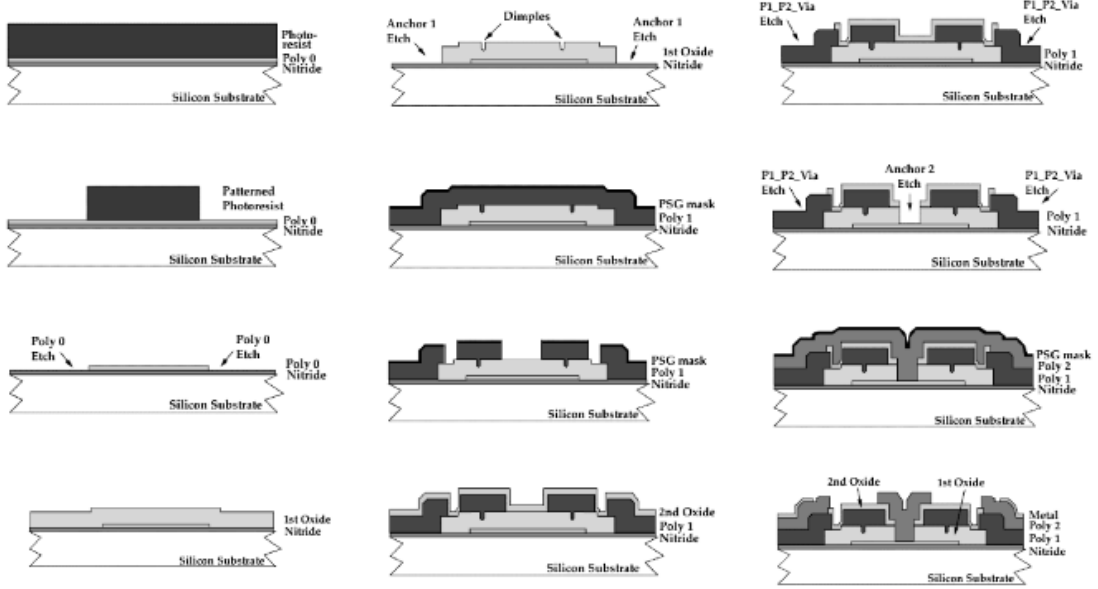


Figure 5.2: The fabrication steps of the three-layer MUMPs technology.

The first step of the fabrication process is deposition of a 600 *nm* low-stress Silicon Nitride layer on the silicon n-type (100) wafers as an electrical isolation layer. This is followed directly by the deposition of the first structural polysilicon film, Poly0, which is 500 *nm* thick. Poly0 is then photolithographically patterned: The Poly0 layer is first coated with photoresist. Then, photoresist is exposed with the first level mask (Poly0), and the exposed photoresist is developed to create the desired etch mask for subsequent pattern transfer to the underlying layer. After patterning the photoresist, the uncovered areas of the Poly0 layer is etched in an RIE (Reactive Ion Etch) system. The remaining photoresist is stripped away.

A 2.0 μm phosphosilicate glass (PSG) sacrificial layer is then deposited by LPCVD. This sacrificial layer of PSG, known as the Oxide layer, is removed at the end of the process to free the first mechanical layer of polysilicon. The sacrificial layer is lithographically patterned with the dimples mask and the dimples are transferred into the sacrificial PSG layer by RIE. The wafers are then patterned with the third mask layer, the anchor mask, and reactive ion etched. This step provides anchor holes that will be filled by the second polysilicon layer (Poly1). After etching anchors, the second structural layer of polysilicon is deposited. This structural layer has a thickness of 2.0 μm , and the moving structures including the proof mass, suspension system and the capacitors are formed in this layer. The polysilicon is

lithographically patterned using a mask designed to form the second structural layer POLY1. After etching the polysilicon, the photoresist is stripped.

The same procedure is followed to form the second sacrificial layer Oxide2 and the third structural layer Poly2. Throughout these steps, appropriate masks are used to form Anchor2 and Poly1-Poly2-Via structures. Finally, the wafer is diced, and the structures are released in HF Solution. Design rules to guarantee an error-free design, including minimum feature sizes, minimum gaps and etching hole specifications are available in the MUMPs Design Handbook by Cronos/JDS Uniphase [25].

5.1.2 Design Implementation Using MUMPs Technology

In the presented design, the proof masses and the flexures are formed in Poly1 with a $2\mu m$ thickness. The total footstep areas of the proof masses were calculated to achieve the required mass assuming a structural thickness of $2\mu m$ and a density of $2.33 \times 10^3 kg/m^3$:

$$m_1 = A_1 t \rho, \quad m_2 = A_2 t \rho, \quad (5.1)$$

where A_1 and A_2 are the footstep areas of the masses m_1 and m_2 , respectively, t is the structural thickness, and ρ is the density of Polysilicon. Since the first sacrificial layer, Oxide1, has a thickness of $2\mu m$, the masses are suspended over the substrate with a $2\mu m$ clearance.

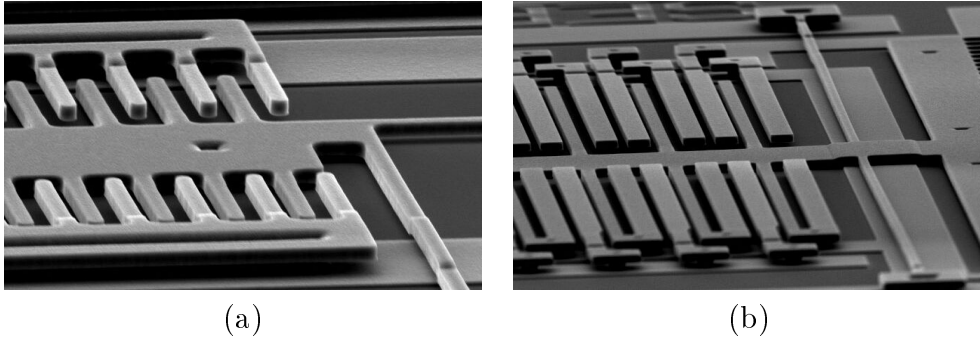


Figure 5.3: Scanning Electron Microscope (SEM) photograph of (a) the comb-drives, and (b) the air-gap sense capacitors.

Interdigitated comb-drives structures which are used to drive the first mass into oscillations in the drive direction are formed in Poly1 (Figure 5.3a). The air-gap capacitors which are used to sense the response of the second mass in the sense direction are also formed in Poly1. The SEM photograph of the air-gap capacitor array built around the second mass is given in Figure 5.3b. Parallel-plate capacitors are used to tune the response of the system, which are also formed in Poly1. The comb-drives, the air-gap capacitors, the parallel-plate capacitors, and the anchors grounding the proof masses are connected to the bonding-pads by connection lines formed in Poly0.

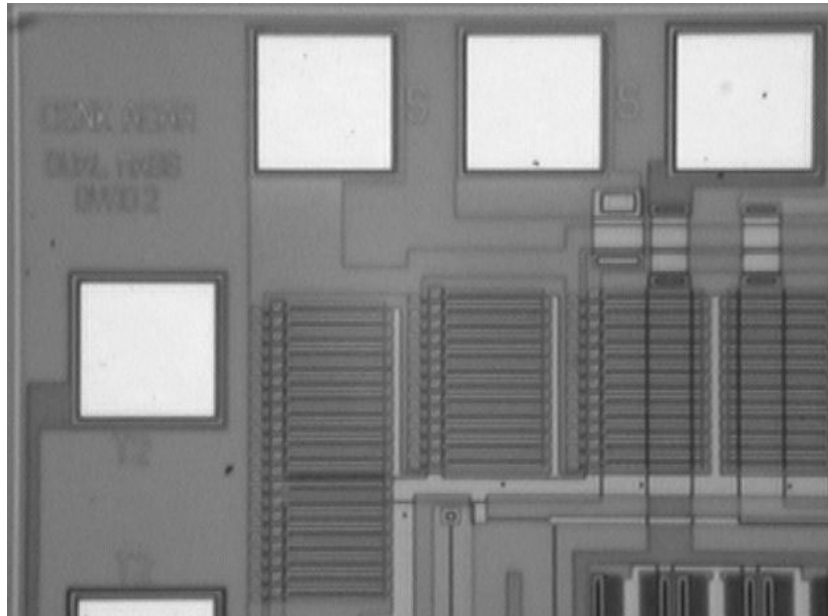
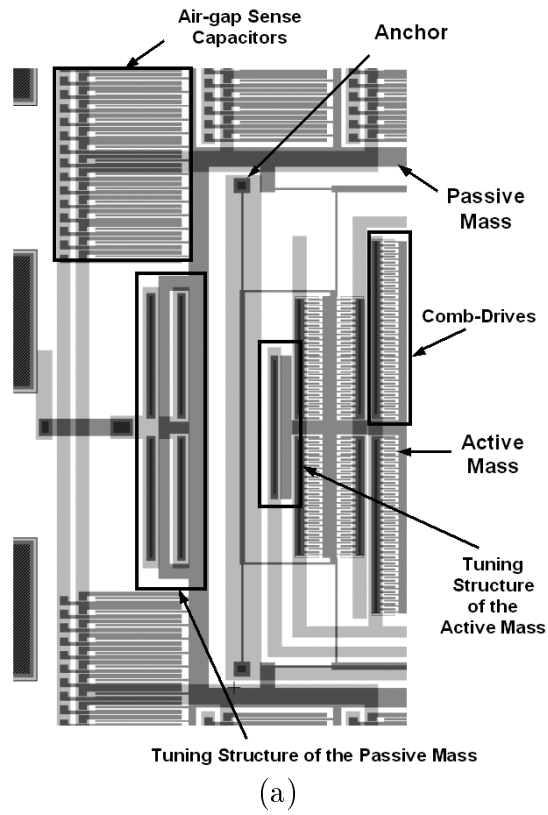


Figure 5.4: (a) The detailed view of the dual-mass z-axis gyroscope layout. (b) The microscope photograph of the gyroscope prototype.

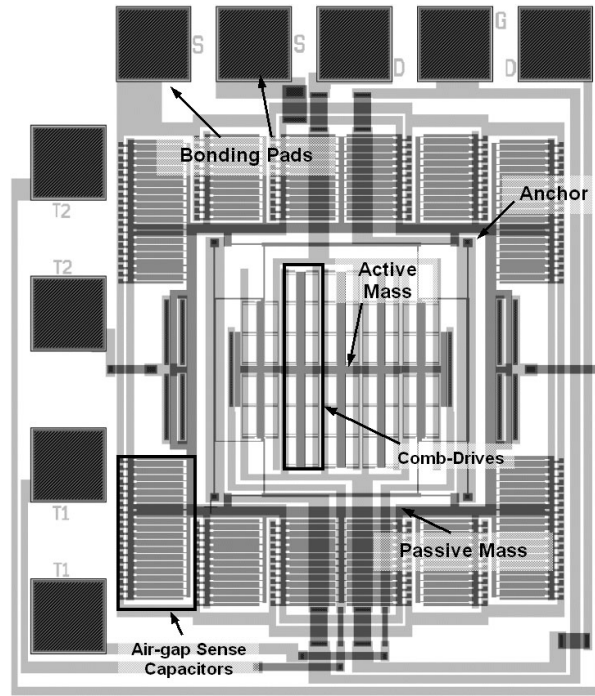


Figure 5.5: The layout of the dual-mass z-axis gyroscope.

5.2 The Experimental Setup

For the preliminary experimental evaluation of the 4-DOF gyroscope designs, first one-sided comb-drive strategy was used to drive the system into oscillations in the drive-mode. This driving scheme can be realized using the setup illustrated in Figure 5.6, where the moving structure is pulled to a DC potential, and a sinusoidal AC voltage is applied to the combs on one side.

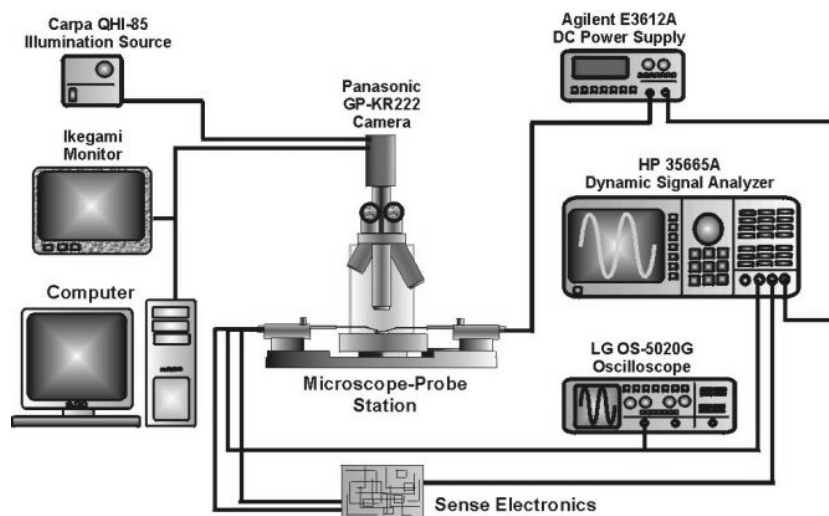


Figure 5.6: Experimental setup for experimental evaluation of prototype gyroscopes.

The initial measurements for the preliminary experiments demonstrating the drive-direction characteristics were taken using computer vision. Even though an accuracy of close to $0.1\mu m$ was achieved in these measurements, the accuracy can be improved using a stroboscope at the correct frequency in the illumination setup, or by employing capacitive sensing electronics in the drive direction.

5.3 Preliminary Experimental Verification of the Design Concept

The Coriolis force which excites the second mass in the sense direction is described by

$$F_{Coriolis} = 2m_2\Omega\dot{x}_2 = 2m_2\Omega\omega_d x_{2o}. \quad (5.2)$$

where ω_d is the driving frequency, and x_{2o} is the oscillation amplitude of the passive mass in the drive direction. Since the Coriolis force is proportional to the linear velocity of the second mass, it is also proportional to the oscillation amplitude. To assure an accurate angular rate measurement, the drive mode oscillation amplitude of the second mass should be kept constant by the drive electronics. Thus, to assure an accurate angular rate measurement, it is crucial that the sensing element of the gyroscope is sustained in a constant amplitude oscillation in the drive direction, since the Coriolis response is directly proportional to the drive direction oscillation amplitude.

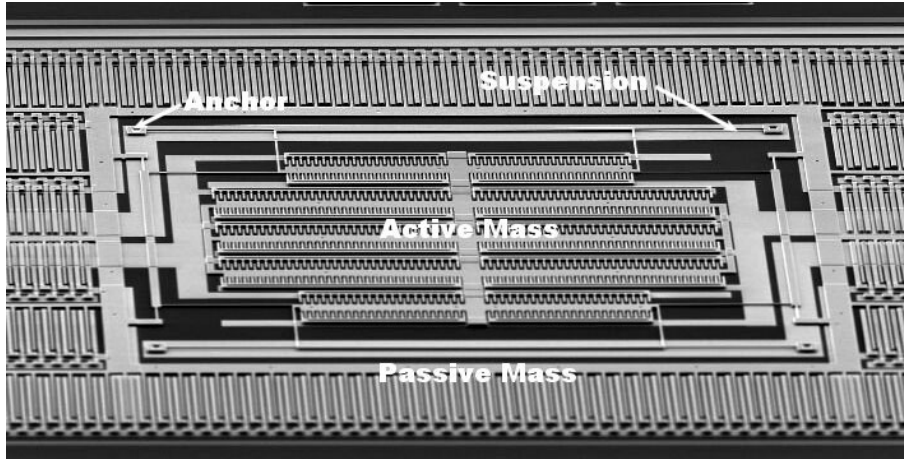


Figure 5.7: Scanning Electron Microscope (SEM) photograph of the tested prototype gyroscope.

Preliminary experiments conducted on prototype dual-mass gyroscopes indicated a driving frequency range of over 2 kHz within where the drive direction oscillation amplitude varies by 10% (Fig. 5.8). A conventional gyroscope design with similar geometry exhibited less than 200 Hz driving frequency range for 10% gain variation under same operating conditions, which is over 1.8 kHz less than dual-mass design operation range, verifying the drastically improved robustness of the dual-mass design.

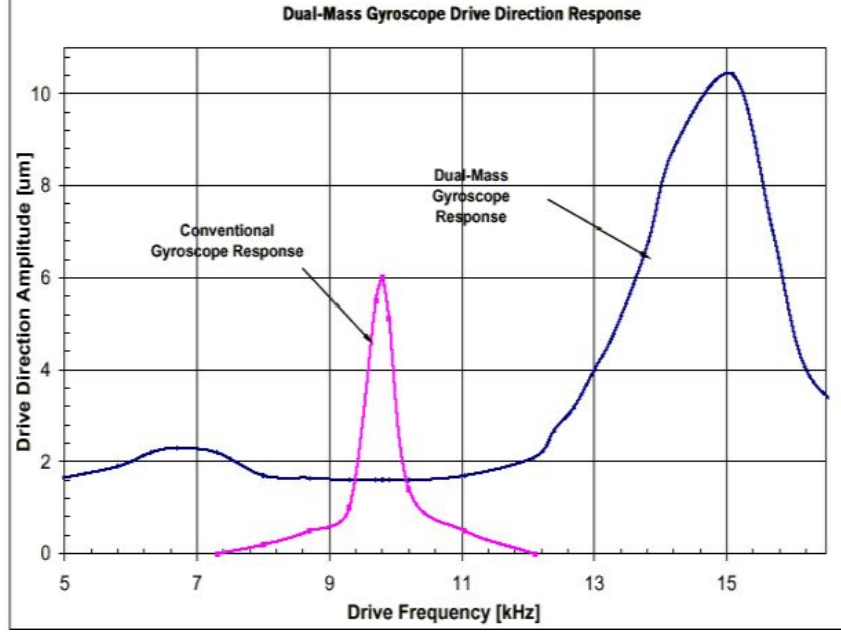


Figure 5.8: Experimental verification of the wide constant-amplitude operation frequency band. 4-DOF system provides a constant-amplitude oscillation frequency band over 10 times larger than conventional gyroscopes under same operation conditions.

The prototype gyroscopes also successfully demonstrated the mechanical amplification of the active mass oscillation by the passive mass, which is the sensing element of the gyroscope. The drive direction oscillation amplitude of the passive mass, which is one of the major parameters determining gyroscope performance, was demonstrated to be over 15 times larger than the active mass under atmospheric pressure (Fig. 5.9). At the antiresonance frequency, the active mass drive amplitude (A_1 in Fig. 5.9) was observed to be less than $0.1\mu m$, while the passive mass amplitude (A_2 in Fig. 5.9) reached $1.4\mu m$.

Moreover, the proposed system offers significant advantages in self-calibration schemes and control of the drive mode oscillations. Since the maximum mechanical amplification occurs at exactly the resonant frequency of the isolated second mass-spring system, the driving frequency was extracted from a reference resonator with the same geometry and parameters as the isolated second mass-spring system built in the vicinity of the dual-mass gyroscope. With a simple Phase-Locked Loop built around the resonator stabilizing the operation frequency to the resonant frequency, the driving signal of the gyroscope is obtained from the output of the voltage-controlled oscillator of the phase-locked loop. Since all parameter variations including residual stresses or fabrication imperfections will reflect on the reference oscillator in the exact same way, the driving frequency of the gyroscope will be locked in the nominal operation band automatically at all times, without the necessity of building feedback loop around the gyroscope itself, significantly simplifying control electronics compared to the conventional designs.

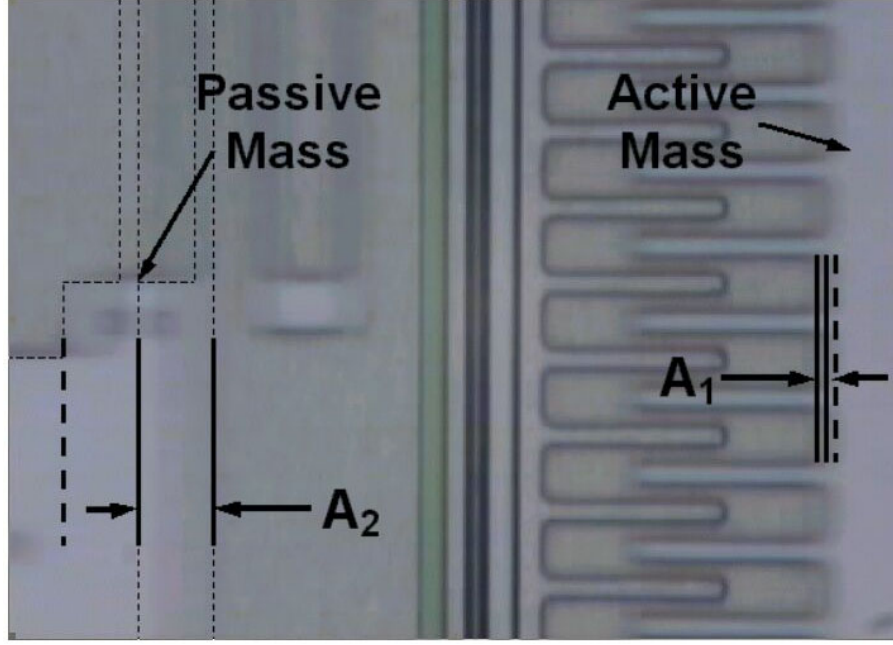


Figure 5.9: Demonstration of mechanical amplification in drive direction. The oscillation blur of the passive mass is highlighted on the left. At the antiresonance frequency, the passive mass amplitude is over an order of magnitude larger than the active mass amplitude.

5.4 Conclusion

In this chapter, MUMPs surface micromachining process, which was selected for fabrication of the prototypes was reviewed; and the design of the prototypes fabricated in the Cronos MUMPs 42 run was presented. After an overview of the used experimental setup, the preliminary experimental results verifying the expected widened operation frequency band of the 4-DOF gyroscope, and the mechanical amplification concept in the drive mode were presented.

Chapter 6

Conclusion and Research Goals

Micromachined gyroscopes could potentially provide high accuracy rotation measurements leading to a wide range of applications including navigation and guidance systems, automotive safety systems, and consumer electronics. However, truly low-cost and high-performance devices are not on the market yet, and the current state of the art micromachined gyroscopes require orders of magnitude improvement in performance, stability, and robustness.

The objective of this research is to develop a novel micromachined vibratory rate gyroscope concept to overcome the limitations of the existing micromachined gyroscope designs. The proposed design concept suggests the use of two coupled independently vibrating proof masses to form a 4-DOF dynamical system. Computer modeling of the proposed design and the experimental results indicated over 15 times increase in the bandwidth of the system as compared to the conventional gyroscopes. In addition, significantly reduced sensitivity of the gyroscope to structural and thermal parameter fluctuations and damping is demonstrated. By utilizing the disturbance-rejection capability of the inertial system, improved robustness is achieved without further sophistication in control electronics. All these advantages of the presented design might relax strict fabrication tolerances and packaging requirements, reducing production cost of micromachined gyroscopes without compromising performance.

6.1 Summary of Achievements

- A detailed analysis of the conventional gyroscope characteristics was carried out, and the limitations due to the resonance-dependent approach were stressed.
- The dynamics of the ideal and non-ideal 4-DOF systems were derived. The phase relations in the ideal and non-ideal 4-DOF system were analyzed to obtain mass trajectories in order to form a basis for developing Quadrature error control strategies.
- An approach for determining optimal dynamical system parameters to maximize sensor performance was developed.

- The sensitivity of the 4-DOF system response to realistic variations in system parameters, including fabrication, pressure, thermal, and residual stress effects, were investigated. In the analysis, the robustness of the proposed system against the parameter variations was compared to a conventional design with a similar geometry.
- A dramatically wider driving frequency range was experimentally demonstrated by fabricated prototype dual-mass gyroscopes within where the drive direction oscillation amplitude varies insignificantly, compared to the conventional gyroscopes.
- Mechanical amplification of driven mass oscillation by the sensing element was also experimentally demonstrated, providing large oscillation amplitudes, which is crucial for sensor performance.
- A trans-resistance amplifier circuit, and an Electromechanical Amplitude Demodulator circuit were built for capacitive measurements of the gyroscope response. The circuits were tested on resonators under vacuum and resonance curves were successfully obtained. However, capacitive detection was not possible for the prototype gyroscope dies in probe station and the wire-bonded gyroscopes; since larger actuation voltages are required compared to resonators under vacuum. Thus, computer vision techniques were used in preliminary experiments.

6.2 Future Goals

- Alternative implementation geometries will be explored, which will provide larger capacitance detection areas with surface micromachining technologies.
- Prototype gyroscopes will also be fabricated in bulk micromachining technologies with much larger structural thickness, which will result in larger actuation and detection capacitances.
- A commercially available capacitive sensing chip in the die form will be wire-bonded to the bulk gyroscope die, and will be packaged together forming a two-chip solution (Fig. 6.1). With this device, the effects of realistic parameter variations on the system response will be experimentally investigated.
- Control strategies for compensation of the quadrature error due to the cross-coupling between the drive and sense directions in the 4-DOF system will be developed, starting from the presented anisoelasticity and phase relations analysis.
- A control system for the drive-mode will be developed, to assure constant amplitude oscillation for the second mass with the required driving frequency.

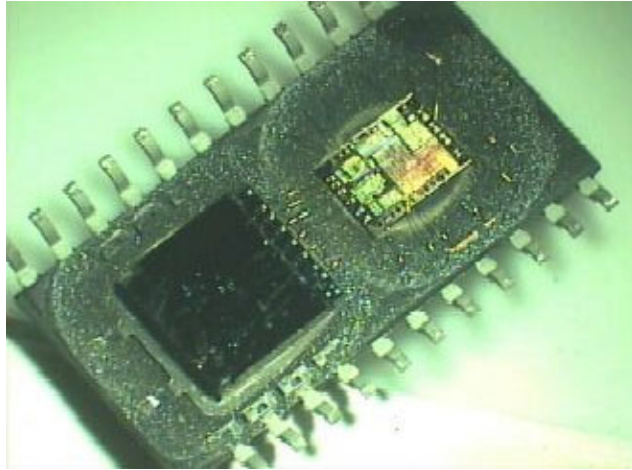


Figure 6.1: A two-chip solution where the capacitive sensing chip in the die form is packaged together with the gyroscope die.

- An analytical approach for optimization of the system parameters for maximizing the sensor performance will be developed.
- A detailed dynamical and structural analysis of the torsional design presented in Figure 3.18 will be carried out, and prototype torsional 4-DOF gyroscopes will be fabricated for experimental verification.

Bibliography

- [1] N. Yazdi, F. Ayazi, and K. Najafi. Micromachined Inertial Sensors. *Proc. of IEEE*, Vol. 86, No. 8, August 1998.
- [2] W.A. Clark. Micromachined Vibratory Rate Gyroscope. *Ph.D. Thesis, BSAC, U.C. Berkeley*, 1994.
- [3] W.A. Clark, R.T. Howe, and R. Horowitz. Surface Micromachined Z-Axis Vibratory Rate Gyroscope. *Proceedings of Solid-State Sensor and Actuator Workshop*, June 1994.
- [4] A. Shkel, R.T. Howe, and R. Horowitz. Micromachined Gyroscopes: Challenges, Design Solutions, and Opportunities. *Int. Workshop on Micro-Robots, Micro-Machines and Systems, Moscow, Russia*, 1999.
- [5] A. Shkel, R. Horowitz, A. Seshia, S. Park and R.T. Howe. Dynamics and Control of Micromachined Gyroscopes *American Control Conference, CA*, 1999.
- [6] US 5,992,233. W.A. Clark. Micromachined z-Axis Vibratory Gyroscope. Nov. 1999.
- [7] US 6,122,961. J.A. Geen, and D.W. Carow. Micromachined Gyros. Sept. 2000.
- [8] US 6,089,089. Y.W. Hsu. Multi-Element Microd Gyro. April 1999.
- [9] J.A. Geen. A Path to Low Cost Gyroscopy. *Solid-State Sensor and Actuator Workshop*, Hilton-Head, SJ, 1998, pp. 51-54.
- [10] C.W. Dyck, J. Allen, and R. Hueber. Parallel Plate Electrostatic Dual Mass Oscillator. *Proceedings of SPIE SOE, CA*, 1999.
- [11] X. Li, R. Lin, and K.W. Leow. Performance-Enhanced Micro-Machined Resonant Systems with Two-Degrees-of-Freedom Resonators. *Journal of Micromech, Microeng.*, Vol. 10, 2000, pp. 534-539.
- [12] T. Usada. Operational Characteristics of Electrostatically Driven Torsional Resonator with Two-Degrees-of-Freedom. *Sensors and Actuators A*, Vol. 64, 1998, pp. 255-257.

- [13] W. Geiger, B. Folkmer, U. Sobe, H. Sandmaier, and W. Lang. New Designs of Micromachined Vibrating Rate Gyroscopes with Decoupled Oscillation Modes. *Sensors and Actuators A*, Vol. 66, 1998, pp. 118-124.
- [14] W. Geiger, W.U. Butt, A. Gaisser, J. Fretch, M. Braxmaier, T. Link, A. Kohne, P. Nommensen, H. Sandmaier, and W. Lang. Decoupled Microgyros and the Design Principle DAVED. *IEEE Sensors Journal*, 2001, pp. 170-173.
- [15] Y. Mochida, M. Tamura, and K. Ohwada. A Micromachined Vibrating Rate Gyroscope with Independent Beams for Drive and Detection Modes. *Sensors and Actuators A*, Vol. 80, 2000, pp. 170-178.
- [16] M. Niu, W. Xue, X. Wang, J. Xie, G. Yang, and W. Wang. Design and Characteristics of Two-Gimbals Micro-Gyroscopes Fabricated with Quasi-LIGA Process. *International Conference on Solid-State Sensor and Actuators*, 1997, pp. 891-894.
- [17] U. Breng, W. Guttman, P. Leinfelder, B. Ryrko, S. Zimmermann, D. Billep, T. Gessner, K. Hillner, and M. Weimer. A Bulk Micromachined Gyroscope Based on Coupled Resonators. *International Conference on Solid-State Sensor and Actuators*, Japan, 1999, pp. 1570-1573.
- [18] E. Netzer, and I. Porat. A Novel Vibratory Device for Angular Rate Measurement. *Journal of Dynamic Systems, Measurement and Control*, Dec. 1995.
- [19] A. Seshia. Design and Modeling of a Dual Mass SOI-MEMS Gyroscope. *M.S. Thesis, BSAC, U.C. Berkeley*, 1999.
- [20] C. Acar, A. Shkel. A Design Approach for Robustness Improvement of Rate Gyroscopes. *Modeling and Simulation of Microsystems Conference*, March 2001.
- [21] C. Acar, A. Shkel. Microgyroscopes with Dynamic Disturbance Rejection. *SPIE Conference on Smart Electronics and MEMS*, March 2001.
- [22] C. Acar, S. Eler, and A. Shkel. Concept, Implementation, and Control of Wide Bandwidth MEMS Gyroscopes. *American Control Conference*, June 2001.
- [23] C. Acar, A. Shkel. Design Concept and Preliminary Experimental Demonstration of MEMS Gyroscopes with 4-DOF “Master-Slave” Architecture. *SPIE Conference on Smart Electronics and MEMS*, March 2002.
- [24] C. Acar and A. Shkel. Wide Bandwidth Micromachined Gyroscope to Measure Rotation. *Patent pending, UCI Office of Technology Alliances*, Case No:2001-140-1.

- [25] D.A. Koester, R. Mahadevan, B. Hardy, and K.W. Markus. MUMPs Design Handbook, Revision 5.0. *Cronos Integrated Microsystems*, 2000.
- [26] W.C. Young. Roark's Formulas for Stress & Strain. *McGraw-Hill, Inc.*, 93-156, 1989.
- [27] W. C. Tang. Electrostatic Comb-Drive for Resonant Sensor and Actuator Applications. *Ph.D. Thesis, University of California at Berkeley*, 1990.
- [28] W. Kuehnel. Modeling of the Mechanical Behavior of a Differential Capacitor Acceleration Sensor. *Sensors and Actuators A*, Vol. 48, 1995, pp. 101-108.
- [29] B.E. Boser. Electronics For Micromachined Inertial Sensors. *Proc. Transducers*, 1997.
- [30] L. Lin, R.T. Howe, and A.P. Pisano. Microelectromechanical Filters for Signal Processing. *Journal of Microelectromechanical Systems*, Vol. 7, Sept. 1998.
- [31] Lemkin. Micro Accelerometer Design with Digital Feedback Control. *Ph.D. Thesis, BSAC, U.C. Berkeley*, 1997.
- [32] A. Shkel, R.T. Howe, and R. Horowitz. Modeling and Simulation of Micromachined Gyroscopes in the Presence of Imperfections. *International Conference on Modeling and Simulation of Microsystems*, Puerto Rico, 1999, pp. 605-608.